



**Calhoun: The NPS Institutional Archive**  
**DSpace Repository**

---

Theses and Dissertations

1. Thesis and Dissertation Collection, all items

---

1987-12

## High Reynolds number

Cowles, Lisa J.

---

<http://hdl.handle.net/10945/22825>

---

This publication is a work of the U.S. Government as defined in Title 17, United States Code, Section 101. Copyright protection is not available for this work in the United States.

*Downloaded from NPS Archive: Calhoun*



<http://www.nps.edu/library>

Calhoun is the Naval Postgraduate School's public access digital repository for research materials and institutional publications created by the NPS community. Calhoun is named for Professor of Mathematics Guy K. Calhoun, NPS's first appointed -- and published -- scholarly author.

**Dudley Knox Library / Naval Postgraduate School**  
**411 Dyer Road / 1 University Circle**  
**Monterey, California USA 93943**



STUDENT ID: 123456789  
NAME: JOHN DOE  
ADDRESS: 12345 MAIN ST, CLEVELAND, OH 44101-1234

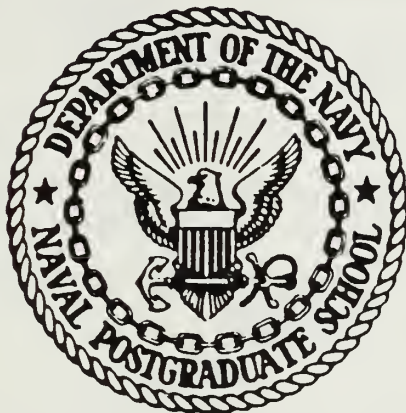






# NAVAL POSTGRADUATE SCHOOL

## Monterey, California



C756965

# THESIS

HIGH REYNOLDS NUMBER, LOW MACH NUMBER,  
STEADY FLOW FIELD CALCULATIONS  
OVER A NACA 0012 AIRFOIL USING  
NAVIER-STOKES AND INTERACTIVE  
BOUNDARY LAYER THEORY

by

Lisa J. Cowles

December 1987

Thesis Advisor:

Max Platzer

Approved for public release; distribution is unlimited

T238784



## REPORT DOCUMENTATION PAGE

1a REPORT SECURITY CLASSIFICATION UNCLASSIFIED			1b RESTRICTIVE MARKINGS		
2a. SECURITY CLASSIFICATION AUTHORITY			3 DISTRIBUTION / AVAILABILITY OF REPORT Approved for public release; distribution is unlimited		
2b. DECLASSIFICATION / DOWNGRADING SCHEDULE					
4 PERFORMING ORGANIZATION REPORT NUMBER(S)			5 MONITORING ORGANIZATION REPORT NUMBER(S)		
6a. NAME OF PERFORMING ORGANIZATION  Naval Postgraduate School		6b OFFICE SYMBOL (If applicable) Code 67		7a NAME OF MONITORING ORGANIZATION  Naval Postgraduate School	
6c. ADDRESS (City, State, and ZIP Code)  Monterey, California 93943-5000			7b. ADDRESS (City, State, and ZIP Code)  Monterey, California 93943-5000		
8a. NAME OF FUNDING / SPONSORING ORGANIZATION		8b. OFFICE SYMBOL (If applicable)		9. PROCUREMENT INSTRUMENT IDENTIFICATION NUMBER	
8c. ADDRESS (City, State, and ZIP Code)			10 SOURCE OF FUNDING NUMBERS		
			PROGRAM ELEMENT NO.	PROJECT NO.	WORK UNIT ACCESSION NO.
11. TITLE (Include Security Classification) HIGH REYNOLDS NUMBER, LOW MACH NUMBER, STEADY FLOW FIELD CALCULATIONS OVER A NACA 0012 AIRFOIL USING NAVIER-STOKES AND INTERACTIVE BOUNDARY LAYER THEORY					
12 PERSONAL AUTHOR(S) Cowles, Lisa J.					
13a. TYPE OF REPORT Master's Thesis		13b TIME COVERED FROM _____ TO _____		14. DATE OF REPORT (Year, Month, Day) 1987, December	
15 PAGE COUNT 118					
16. SUPPLEMENTARY NOTATION					
17. COSATI CODES			18. SUBJECT TERMS (Continue on reverse if necessary and identify by block number)		
FIELD	GROUP	SUB-GROUP	Navier-Stokes, Interactive Boundary Layer theory, lift coefficient, pressure coefficient, skin friction coefficient, velocity profiles		
19. ABSTRACT (Continue on reverse if necessary and identify by block number)					
<p>A Navier-Stokes code, developed by N.L. Sankar, and an Interactive Boundary Layer code, developed by Tuncer Cebeci, are implemented for high Reynolds number, low Mach flows over a NACA 0012 airfoil. Upper surface pressure distributions, coefficients of lift, coefficients of friction, and velocity profiles obtained from the Navier-Stokes code are compared to results obtained from the Cebeci Interactive Boundary Layer code for steady flow. The steady state cases investigated are at .3 Mach and Reynolds numbers of 1 to 15 million, and at .12 Mach and a Reynolds number of 1.5 million.</p>					
20 DISTRIBUTION / AVAILABILITY OF ABSTRACT <input checked="" type="checkbox"/> UNCLASSIFIED/UNLIMITED <input type="checkbox"/> SAME AS RPT <input type="checkbox"/> DTIC USERS			21 ABSTRACT SECURITY CLASSIFICATION Unclassified		
22a NAME OF RESPONSIBLE INDIVIDUAL Prof. Max Platzer			22b TELEPHONE (Include Area Code) (408) 646-2311		22c. OFFICE SYMBOL Code 67Pl



Approved for public release; distribution is unlimited

High Reynolds Number, Low Mach Number, Steady  
Flow Field Calculations Over a NACA  
0012 Airfoil Using Navier-Stokes and Interactive  
Boundary Layer Theory

by

Lisa J. Cowles  
Civilian, Naval Air Development Center  
B.S., The Pennsylvania State University, 1983  
B.A., Lycoming College, 1982

Submitted in partial fulfillment of the  
requirements for the degree of

MASTER OF SCIENCE IN  
AERONAUTICAL ENGINEERING

from the

NAVAL POSTGRADUATE SCHOOL  
December 1987

## ABSTRACT

A Navier-Stokes code, developed by N.L. Sankar, and an Interactive Boundary Layer code, developed by Tuncer Cebeci, are implemented for high Reynolds number, low Mach flows over a NACA 0012 airfoil. Upper surface pressure distributions, coefficients of lift, coefficients of friction, and velocity profiles obtained from the Navier-Stokes code are compared to results obtained from the Cebeci Interactive Boundary Layer code for steady flow. The steady state cases investigated are at .3 Mach and Reynolds numbers of 1 to 15 million, and at .12 Mach and a Reynolds number of 1.5 million.

*Tesis*  
*C756965*  
*2.1*

## TABLE OF CONTENTS

I.	INTRODUCTION -----	1
II.	OBJECTIVES -----	5
III.	MATHEMATICAL FORMULATION -----	7
	A. GOVERNING EQUATIONS -----	7
	B. REYNOLDS STRESSES -----	12
	C. TURBULENCE MODELING -----	16
IV.	THE BOUNDARY LAYER EQUATION -----	23
V.	THE SANKAR NAVIER-STOKES METHOD -----	27
	A. GRID GENERATION -----	27
	B. INITIAL CONDITIONS AND BOUNDARY CONDITIONS --	33
	C. NUMERICAL FORMULATION -----	36
	D. USE OF SANKAR'S N-S CODE -----	47
VI.	THE CEBECI INTERACTIVE BOUNDARY LAYER METHOD ----	51
	A. VISCOUS INNER FLOW -----	52
	B. INVISCID OUTER FLOW -----	57
	C. STRONG INTERACTION MODEL -----	58
	D. USE OF CEBECI'S IBL CODE -----	59
VII.	PRESENTATION OF COMPUTATIONS -----	63
VIII.	RESULTS AND DISCUSSION -----	97
IX.	CONCLUSIONS AND RECOMMENDATIONS -----	101
	LIST OF REFERENCES -----	103
	INITIAL DISTRIBUTION LIST -----	106

## LIST OF TABLES

5.1	INPUT PARAMETERS FOR THE SANKAR N-S CODE -----	49
5.2	VALUES USED FOR THE SANKAR N-S CODE -----	50
6.1	INPUT PARAMETERS FOR THE CEBECI IBL CODE -----	61
6.2	VALUES USED FOR THE CEBECI IBL CODE -----	62



## LIST OF FIGURES

3.1	The Flux of Mass Through a Cube -----	8
3.2	X-components of Surface Forces on an Element ----	10
4.1	Velocity Profile -----	24
5.1	Defined Points on the Airfoil Surface -----	29
5.2	Symmetric Airfoil in the Physical Plane -----	30
5.3	Symmetric Airfoil Unwrapped in the Intermediate Plane -----	31
5.4	Far Field Boundaries -----	32
5.5	Final Grid in the Physical Plane -----	34
5.6	Detail of Grid Around the Airfoil -----	35
7.1	$C_\ell$ vs AOA; $Re = 6M$ , $N-S M = .3$ -----	64
7.2	$C_\ell$ vs AOA; $Re = 1.5M$ , $N-S M = .12$ -----	65
7.3	$C_p$ vs $x/c$ ; $AOA = 0$ , $N-S M = .3$ -----	67
7.4	$C_p$ vs $x/c$ ; $Re = 6M$ , $N-S M = .3$ -----	68
7.5	$C_p$ vs $x/c$ ; $Re = 1.5M$ , $N-S M = .12$ -----	69
7.6	$C_f$ vs $x/c$ ; $Re = 6M$ , $AOA = 0$ , $N-S M = .3$ -----	70
7.7	$C_f$ vs $x/c$ ; $Re = 3M$ , $AOA = 0$ , $N-S M = .3$ -----	73
7.8	$C_f$ vs $x/c$ ; $Re = 15M$ , $AOA = 0$ , $N-S M = .3$ -----	74
7.9	Velocity Profile; IBL, $Re = 6M$ , $AOA = 0$ , Trans. $.005c$ -----	75
7.10	Velocity Profile; IBL, $Re = 6M$ , $AOA = 0$ , Trans. $0.70c$ -----	76
7.11	Velocity Profile; N-S, $Re = 6M$ , $AOA = 0$ , $M = .3$ 1st Grid Point $.0001c$ -----	77
7.12	Velocity Profile; N-S, $Re = 6M$ , $AOA = 0$ , $M = .3$ , 1st Grid Point $.00002$ -----	78

7.13	Velocity Profile; IBL, Re = 15M, AOA = 0, Trans. .005c -----	79
7.14	Velocity Profile; N-S, Re = 15M, AOA = 0, M = .3, 1st Grid Point .0001c -----	80
7.15	Velocity Profile; N-S Re = 15M, AOA = 0, M = .3, 1st Grid Point .000005c -----	81
7.16	Velocity Profile; IBL, Re = 1M, AOA = 0, Trans. = .005c -----	82
7.17	Velocity Profile; N-S, Re = 1M, AOA = 0, M = .3, 1st Grid Point .0001c -----	83
7.18	$C_f$ vs $x/c$ ; IBL, AOA = 0, Trans. .005c -----	85
7.19	$C_f$ vs $x/c$ ; N-S, AOA = 0, M = .3 -----	86
7.20	$C_f$ vs $x/c$ ; IBL and N-S, RE = 3, 6, 15M, AOA = 0, N-S M = .3, IBL Trans. .005c -----	87
7.21	$C_f$ vs $x/c$ ; IBL, Re = 6M, Trans .005c -----	89
7.22	$C_f$ vs $x/c$ ; N-S, Re = 6M, M = .3, 1st Grid Point .0001c -----	90
7.23	$C_f$ vs $x/c$ ; N-S, Re = 6M, M = .3, 1st Grid Point .00001c -----	91
7.24	$C_f$ vs $x/c$ ; IBL and N-S, Re = 6M, AOA = 12, N-S M = .3, IBL Trans. .005c -----	92
7.25	$C_f$ vs $x/c$ ; IBL; Re = 1.5M, Trans. .005c -----	93
7.26	$C_f$ vs $x/c$ ; N-S; Re = 1.5M, M = .12, 1st Grid Point .0001 -----	94
7.27	$C_f$ vs $x/c$ ; N-S; Re = 1.5M, M = .12, 1st Grid Point .00005 -----	95
7.28	$C_f$ vs $x/c$ ; IBL and N-S, Re = 1.5M, AOA = 6, N-S M = .12, IBL Trans. .005c -----	96

## LIST OF SYMBOLS

$a$	acceleration
$A$	area, parameter used in Cebeci-Smith and Baldwin-Lomax turbulence model
$A, B$	Jacobian matrices
$c$	airfoil chord length
$C_f$	skin friction coefficient
$C_l$	lift coefficient
$C_p$	pressure coefficient
$D$	artificial dissipation
$e$	total energy per unit volume
$E$	energy
$\vec{E}, \vec{F}$	convection vectors in physical plane
$E, F$	convection vectors in computational plane
$F$	force, ratio of normal stress turbulent energy to shear stress turbulent energy
$F_{wake}$	wake function
$F_{Kleb}$	Klebanoff intermittancy factor
$G_{\gamma tr}$	empirical constant used in Cebeci-Smith turbulence model
$I$	identity matrix
$J$	transformation Jacobian flux of momentum
$L$	linear dimension of the body
$m$	mass
$M_\infty$	freestream Mach number
$p$	pressure

$q$	flow-field vector
$R$	Reynolds number, Boltzman constant
$R_x$	length Reynolds number
$R_\theta$	Reynolds number based on momentum thickness
$Re_{\gamma tr}$	transitional Reynolds number
$\vec{R}, \vec{S}$	diffusion vectors in physical plane
$R, S$	diffusion vectors in computational plane
$t$	time
$T$	temperature
$U$	velocity
$U_e$	boundary layer edge velocity
$U_0$	reference velocity
$u, v, w$	velocity components in physical plane
$V$	freestream velocity
$W$	work
$x, y$	coordinates in physical plane
$z$	complex coordinate representation of a point in the physical plane
$\alpha$	angle of incidence (attack) parameter used in Cebeci-Smith turbulence model
$\beta$	ratio of time averaged quantities
$\gamma$	damping function used in Cebeci-Smith turbulence model, ratio of specific heat
$\gamma_{tr}$	intermittancy factor used in Cebeci-Smith turbulence model
$\delta$	boundary layer thickness
$\delta^*$	displacement thickness



$\epsilon$	function of maximum pressure gradient dissipation used in Baldwin-Lomax turbulence model
$\zeta$	complex coordinate representation of a point in the computational plane
$\eta$	Falkner-Skan transformation
$\mu$	viscosity
$\nu$	kinematic viscosity
$\nu_t$	eddy viscosity
$\xi, \eta$	coordinates in transformed plane
$\rho$	density
$\sigma_x, \sigma_y, \sigma_z$	stress terms
$\tau_{xx}, \tau_{xy}, \dots$	stress terms
$\tau_w$	shear stress at the wall
$\Phi$	perturbation potential
$\psi$	stream function
$\omega$	vorticity

#### Operators:

$\delta$	partial difference central difference
$\Delta$	incremental change
$\nabla$	del operator

## ACKNOWLEDGEMENTS

I would like to express my sincere appreciation to my thesis advisor, Dr. Platzer. His knowledge of, and interest in, aerodynamics has been a tremendous inspiration to me. Professor Platzer's guidance throughout my studies has been extremely beneficial, both in my thesis work and in my ability to successfully accomplish future projects.

I would like to thank Dr. Larry Carr at NASA Ames for all of his advice and suggestions and Joan Thompson, Charles Hooper, and others at Sterling Software who were invaluable with their help in using NASA's Vaxes and Cray. Andreus Krainer at the Naval Postgraduate School deserves special thanks for his hours of assistance. Also, in appreciation, I would like to thank Dennis Huff at NASA Lewis and Dr. Sankar for their time during phone conversations and their advice on the use of the Navier-Stokes based code.



## I. INTRODUCTION

Computational fluid dynamics has matured significantly within the past decade because of the development of increased computational capabilities and powerful computational techniques. Current problems being addressed include predicting flow separation over airfoils and post-stall flight characteristics. These areas are of interest because studies [Ref. 1] indicate increased lift and thus sustained flight are attainable when an airfoil is dynamically stalled, that is, its angle of attack is pitched to a post stall angle of attack rather than being initially placed at that high lift.

Computational methods utilizing the full Navier-Stokes (N-S) equations are capable of addressing these issues, as are methods that include approximations to the Navier-Stokes equations. One method, the Interactive Boundary Layer (IBL) technique, developed by Tuncer Cebeci at Douglas Aircraft Company and at the California State University [Ref. 2], divides the flow over an airfoil into a viscous inner boundary layer and an inviscid outer layer. The characteristics of the inner flow are obtained from a numerical solution of Prandtl's boundary layer equation and the outer flow's characteristics are determined from Hess and Smith's panel method, and Fourier analysis and conformal



mapping. The inner and outer layers are then redetermined by an interaction model that iterates between the two regions and marches downstream until the flow conditions have been satisfied at the boundary for both regions. The Cebeci IBL code uses Michel's criterion to predict transition from laminar to turbulent flow or transition may be prescribed. An algebraic (Cebeci-Smith) turbulence model is used.

A full Navier-Stokes code developed by N.L. Sankar and his associates at the Georgia Institute of Technology [Ref. 3] uses an implicit finite-difference procedure to solve the 2-D Reynolds-averaged compressible Navier-Stokes equations in strong conservative form. The time-marching algorithm used is an Alternating Direction Implicit (ADI) procedure developed by Beam and Warming [Ref. 4] and implemented by Steger [Ref. 5]. The Sankar N-S code uses a body-fitted C-grid system and an algebraic (Baldwin-Lomax) turbulence model.

The Cebeci IBL and the Sankar N-S codes are designed for different purposes. A low Reynolds number flow over an airfoil tends to be laminar until separation. The flow then transitions to turbulent flow and reattaches as turbulent flow. The Cebeci IBL code models this separation bubble if transition is specified within the separation bubble. Velocity profiles and skin coefficients are extremely important in analyzing these low Reynolds flows. Cebeci has

developed codes for compressible oscillating airfoils, however, this Cebeci IBL code was developed for incompressible steady state flow only and thus does not predict the effects of unsteady flow nor compressibility.

The Sankar N-S code was developed to address dynamic stall and its implication of increased lift. Therefore, the values of interest to date have been coefficients of pressure, lift, moment, and the effect of hysteresis on these values. However, the Sankar N-S code assumes the flow is fully turbulent, and therefore does not account for transition from laminar to turbulent flow.

Neither dynamic stall nor transition within a separation bubble are easily quantified experimentally. Transition is a boundary layer phenomenon and the velocity profiles and skin frictions within the boundary layer must be measured to assure correct interpretation of the flow under investigation; surface pressures are not sufficient to accurately locate flow separation and reattachment [Ref. 6]. This is a time consuming, expensive process prone to error. Experimental methods include laser anemometry and hot wire probes [Ref. 7]. Disturbance of the boundary layer flow due to probes is undesirable and hot wire probes are normally unable to determine flow direction; therefore laser anemometry, although expensive and tedious, is increasingly being used.

Dynamic stall is difficult to characterize due to the transitory nature of the phenomenon. Experimental techniques and apparatus include pressure transducers, hot wire probes, and laser doppler velocimetry [Ref. 8]. Flow visualization is also a very effective tool for studying both dynamic stall and separation bubbles [Refs. 9,10].

A good review of the current state-of-the-art computational and experimental aspects of aerodynamic flows is given in the proceedings of three symposia on this topic edited by T. Cebeci [Ref. 11].

## II. OBJECTIVES

The intent of this study is two-fold: to become familiar with computational fluid dynamic methods and to evaluate two codes to determine their range of applicability.

Computational fluid dynamics consists of various mathematical methods and implementation schemes. A significant portion of analysis inherent in computational codes is empirical; therefore, the assumptions used strongly influence the results. It is important, when attempting to choose a computational code for a specific purpose, to be familiar with the significance of the analytical methods, assumptions made, and empirical models. Each code is different in these respects and must be analyzed individually and in detail to assure reliable, accurate results, especially when extending the flow regime or airfoil to conditions whose features are unknown.

The two codes chosen, the Cebeci IBL code and the Sankar N-S code, are a good representation of two powerful, accurate methods that differ widely in computational approach. The Cebeci IBL code has been extensively tested in a variety of steady state conditions [Ref. 12] and the Sankar N-S code has compared well to experimental data for a pitching airfoil [Ref. 13]. However, the lack of steady



state boundary layer data for the Sankar N-S code indicated that a more in-depth analysis of the applicability of the code was required. The Cebeci IBL code was used as the reference for the Sankar code.

The analysis included the following:

1. Assess  $C_l$  for Reynolds numbers of 1.5 and 6 million
2. Assess  $C_p$  and  $C_f$  for a range of Reynolds numbers (1-15 million at 0 degrees angle of attack) and angles of attack (0, 2, 4, and 6 degrees for 1.5M Re number and 0, 4, 8, and 12 degrees for 6M Re number)
3. Assess velocity profiles for Reynolds numbers of 1, 6, and 15 million
4. Assess the influence of dissipation factors and grid size on the results of the Sankar N-S code.

### III. MATHEMATICAL FORMULATION

#### A. GOVERNING EQUATIONS

Flow over an airfoil can be described by the velocity  $\hat{q} = \hat{u}i + \hat{v}j + \hat{w}k$ , the pressure, the density, and the temperature. These six variables ( $u$ ,  $v$ ,  $w$ ,  $p$ ,  $\rho$ , and  $T$ ) are fully described by the continuity equation, the equation of state,  $p = \rho RT$ ; the energy equation,  $\delta Q - \delta W = \delta E$ ; and the three equations of motion. [Ref. 14]

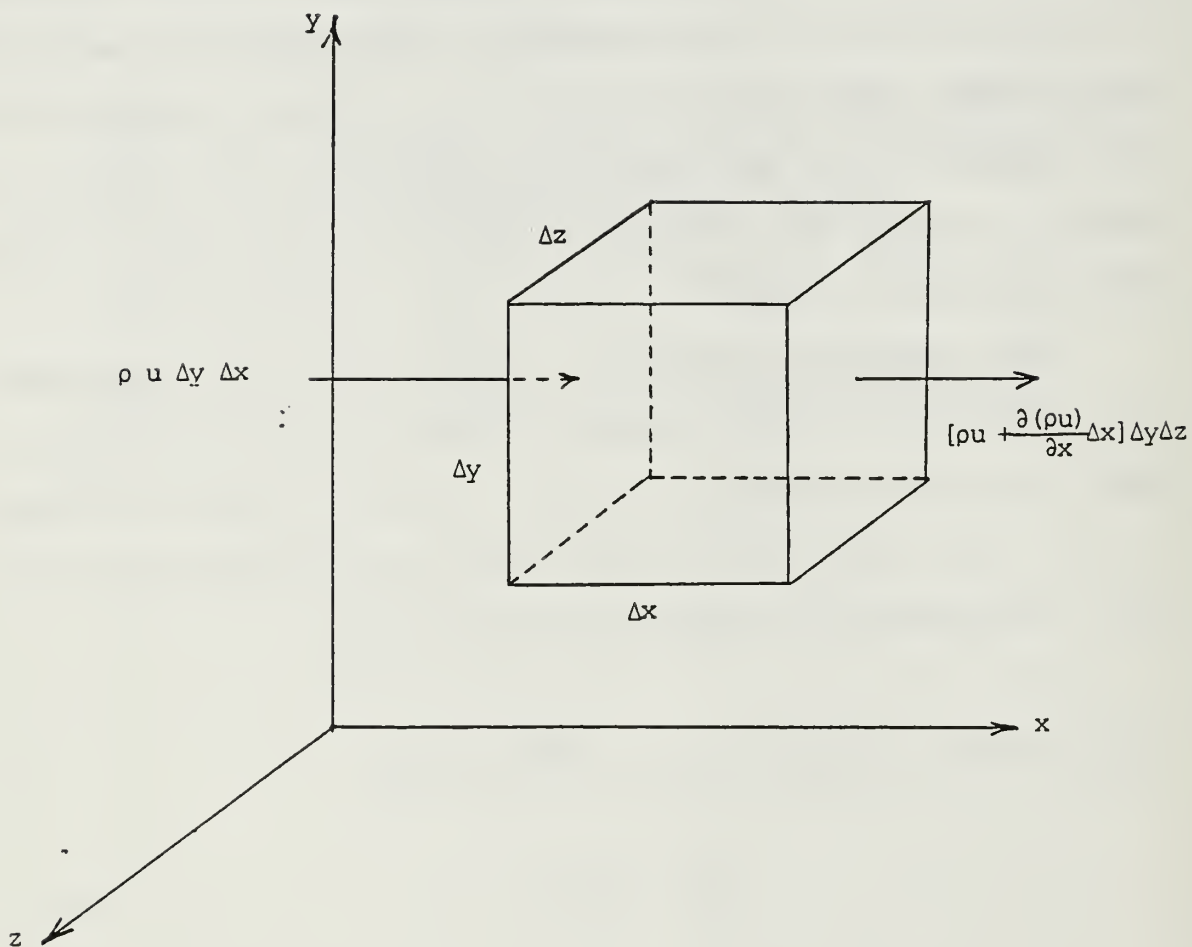
The continuity equation states mass is conserved; i.e., the flux of mass through a cube per time is equal to the time rate of change of mass. This is shown in Figure 3.1 for the flow through the faces perpendicular to the  $x$  axis. Mathematically this is expressed as

$$\begin{aligned} & \left[ \frac{\partial (\rho u)}{\partial x} \Delta x \right] \Delta y \Delta z - \left[ \frac{\partial (\rho v)}{\partial y} \Delta y \right] \Delta z \Delta x - \left[ \frac{\partial (\rho w)}{\partial z} \Delta z \right] \Delta x \Delta y \\ & = \frac{\partial}{\partial t} (\rho \Delta x \Delta y \Delta z) \end{aligned} \quad (3.1)$$

Since the control volume is fixed,  $\Delta x \Delta y \Delta z$  is independent of time; therefore

$$\frac{\partial \rho}{\partial t} + \frac{\partial (\rho u)}{\partial x} + \frac{\partial (\rho v)}{\partial y} + \frac{\partial (\rho w)}{\partial z} = 0, \quad (3.2)$$

or



Net flux through face perpendicular to x-axis

$$= - \left[ \frac{\partial (\rho u)}{\partial x} \Delta x \right] \Delta y \Delta z$$

Source: [Ref. 14:p. 106]

Figure 3.1 The Flux of Mass Through a Cube

$$\frac{\partial \rho}{\partial t} + \Delta \cdot \rho \mathbf{q} = 0 . \quad (3.3)$$

Alternately,

$$\frac{D\rho}{Dt} + \rho \left( \frac{\partial u}{\partial x} + \frac{\partial v}{\partial y} + \frac{\partial w}{\partial z} \right) = 0 \quad (3.4)$$

or

$$\frac{D\rho}{Dt} + \rho (\Delta \cdot \mathbf{q}) = 0 \quad (3.5)$$

The three equations of motion, one for each axis of the Cartesian coordinate system, are described by Newton's second law,  $\Delta \mathbf{F} = \Delta (m\mathbf{a})$ . The summation of the x components of surface forces on the element shown in Figure 3.2 is

$$\Delta F_x = \Delta m a_x = (\rho \Delta x \Delta y \Delta z) \frac{Du}{Dt} \quad (3.6)$$

with

$$\begin{aligned} \Delta F_x = & - \sigma_x \Delta y \Delta z + \left( \sigma_x + \frac{\partial \sigma_x}{\partial x} \Delta x \right) \Delta y \Delta z \\ & - \tau_{yx} \Delta x \Delta z + \left( \tau_{yx} + \frac{\partial \tau_{yx}}{\partial y} \Delta y \right) \Delta x \Delta z \\ & - \tau_{zx} \Delta x \Delta y + \left( \tau_{zx} + \frac{\partial \tau_{zx}}{\partial z} \Delta z \right) \Delta x \Delta y . \end{aligned} \quad (3.7)$$

## STRESS-STRAIN RELATIONS

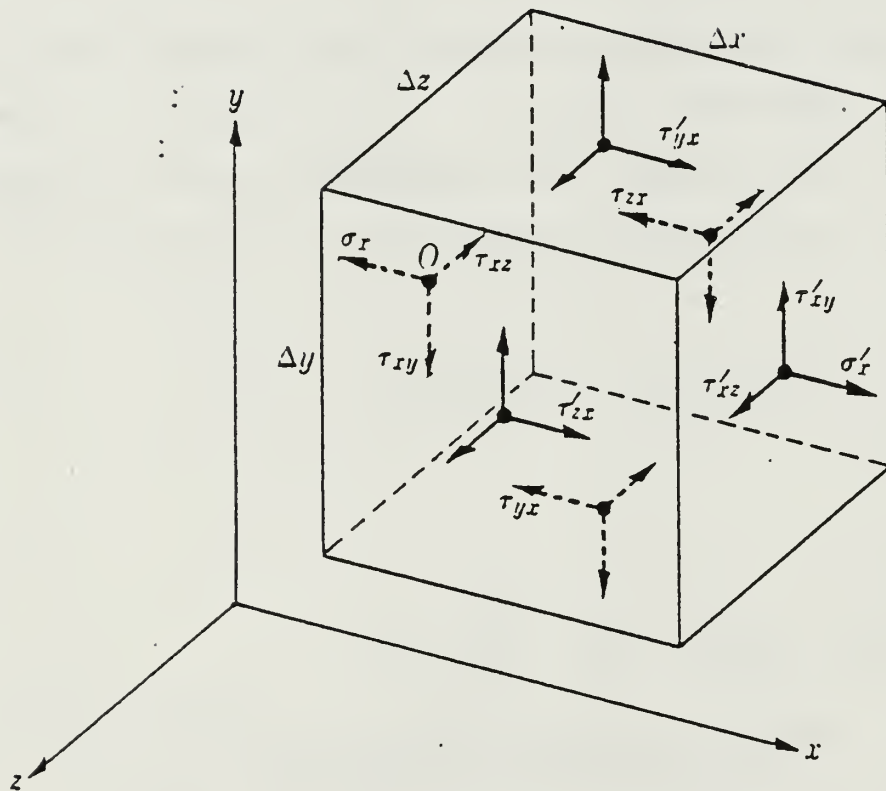


Figure 3.2 X-components of Surface Forces on an Element

Dividing by the volume of the element yields

$$\frac{\partial \sigma_x}{\partial x} + \frac{\partial \tau_{yx}}{\partial y} + \frac{\partial \tau_{zx}}{\partial z} = \rho \frac{Du}{Dt} \quad (3.8)$$

Similarly, for the y and z directions

$$\frac{\partial \sigma_y}{\partial y} + \frac{\partial \tau_{xy}}{\partial x} + \frac{\partial \tau_{zy}}{\partial z} = \rho \frac{Dv}{Dt} \quad (3.9)$$

and

$$\frac{\partial \sigma_z}{\partial z} + \frac{\partial \tau_{xz}}{\partial x} + \frac{\partial \tau_{yz}}{\partial y} = \rho \frac{Dw}{Dt} \quad (3.10)$$

For Newtonian fluids with a single viscosity coefficient, the normal and tangential shear stresses are as follows [Ref. 15]:

$$\sigma_x = -p + 2\mu \frac{\partial u}{\partial x} - \frac{2}{3}\mu (\nabla \cdot \hat{q}) \quad (3.11a)$$

$$\sigma_y = -p + 2\mu \frac{\partial v}{\partial y} - \frac{2}{3}\mu (\nabla \cdot \hat{q}) \quad (3.11b)$$

$$\sigma_z = -p + 2\mu \frac{\partial w}{\partial z} - \frac{2}{3}\mu (\nabla \cdot \hat{q}) \quad (3.11c)$$

$$\tau_{yx} = \tau_{xy} = \mu \left( \frac{\partial v}{\partial x} + \frac{\partial u}{\partial y} \right) \quad (3.11d)$$

$$\tau_{yz} = \tau_{zy} = \mu \left( \frac{\partial w}{\partial y} + \frac{\partial v}{\partial z} \right) \quad (3.11e)$$

$$\tau_{zx} = \tau_{xz} = \mu \left( \frac{\partial u}{\partial z} + \frac{\partial w}{\partial x} \right) \quad (3.11f)$$



Substituting these stress definitions into the equations of motion, and assuming a constant viscosity corresponding to the mean temperature of the fluid ultimately yields the Navier-Stokes equations:

$$-\frac{\partial p}{\partial x} + \mu \left[ \frac{\partial^2 u}{\partial x^2} + \frac{\partial^2 u}{\partial y^2} + \frac{\partial^2 u}{\partial z^2} \right] + \frac{\mu}{3} \frac{\partial}{\partial x} [\nabla \cdot \hat{q}] = \rho \frac{Du}{Dt} \quad (3.12a)$$

$$-\frac{\partial p}{\partial y} + \mu \left[ \frac{\partial^2 v}{\partial x^2} + \frac{\partial^2 v}{\partial y^2} + \frac{\partial^2 v}{\partial z^2} \right] + \frac{\mu}{3} \frac{\partial}{\partial y} [\nabla \cdot \hat{q}] = \rho \frac{Dv}{Dt} \quad (3.12b)$$

$$-\frac{\partial p}{\partial z} + \mu \left[ \frac{\partial^2 w}{\partial x^2} + \frac{\partial^2 w}{\partial y^2} + \frac{\partial^2 w}{\partial z^2} \right] + \frac{\mu}{3} \frac{\partial}{\partial z} [\nabla \cdot \hat{q}] = \rho \frac{Dw}{Dt} \quad (3.12c)$$

or in vector format

$$-\nabla p + \mu \nabla^2 \hat{q} + \frac{\mu}{3} \nabla (\nabla \cdot \hat{q}) = \rho \frac{\partial \hat{q}}{\partial t} + \rho (\hat{q} \cdot \nabla) \hat{q} \quad (3.13)$$

[Ref. 14]

## B. REYNOLDS STRESSES

The Navier-Stokes equations are valid for laminar and turbulent flow. However, the complexity of turbulence has made it impossible to relate the motion of the fluid to the boundary conditions and obtain an exact solution. Therefore, the turbulence must currently be modeled. O. Reynolds divided the turbulent flow into a mean motion and fluctuating, or eddying, motion as follows:

$$u = \bar{u} + u' \quad (3.14a)$$

$$v = \bar{v} + v' \quad (3.14b)$$

$$w = \bar{w} + w' \quad (3.14c)$$

$$p = \bar{p} + p' \quad (3.14d)$$

$$\rho = \bar{\rho} + \rho' \quad (3.14e)$$

$$T = \bar{T} + T' \quad (3.14f)$$

where the barred terms are the time-average of the component and the slashed terms are the fluctuations. By definition, the time averages of all quantities describing the fluctuations are equal to zero:

$$\bar{u}' = 0, \quad \bar{v}' = 0, \quad \bar{w}' = 0, \quad \bar{p}' = 0, \quad \bar{\rho}' = 0, \quad \bar{T}' = 0$$

Rules for operating on mean time-averages are given below.  $F$  and  $g$  are dependent variables, and  $s$  is the independent variable  $x, y, z$ , or  $t$ .

$$\overline{\bar{f}} = \bar{f}$$

$$\overline{\bar{f} + \bar{g}} = \bar{f} + \bar{g}$$

$$\overline{\bar{f} * \bar{g}} = \bar{f} * \bar{g}. \quad [\text{Ref. 16}]$$

The stresses caused by the fluctuations can be determined using the momentum theorem. Consider an area  $dA$  with  $dA * \rho u * dt$  being the mass of incompressible fluid passing through the element in time  $dt$ . Thus, the flux of momentum in the  $x$  direction is

$$dJ_x = dA * \rho u^2 * dt; \quad (3.15a)$$

Correspondingly,

$$dJ_y = dA * \rho uv * dt \quad (3.15b)$$

and

$$dJ_z = dA * \rho uw * dt. \quad (3.15c)$$

Calculating the time averages for the fluxes of momentum per unit time yields:

$$\overline{dJ_x} = dA \rho \overline{u^2} \quad (3.16a)$$

$$\overline{dJ_y} = dA \rho \overline{uv} \quad (3.16b)$$

$$\overline{dJ_z} = dA \rho \overline{uw}. \quad (3.16c)$$

Utilizing the definition of turbulent flow and the previous rules yields

$$\overline{dJ}_x = dA \cdot \rho (\overline{u^2} + \overline{u'^2}) \quad (3.17a)$$

$$\overline{dJ}_y = dA \cdot \rho (\overline{u \cdot v} + \overline{u'v'}) \quad (3.17b)$$

$$\overline{dJ}_z = dA \cdot \rho (\overline{u \cdot w} + \overline{u'w'}) \quad (3.17c)$$

Dividing these rates of change of momentum by area  $dA$ , we obtain stresses. The equal and opposite stresses exerted on the area by the surroundings are a normal stress,  $-(\overline{u^2} + \overline{u'^2})$ , and two shearing stresses,  $-(\overline{uv} + \overline{u'v'})$  and  $-(\overline{uw} + \overline{u'w'})$ . Thus, the superposition of fluctuations on the mean motion gives rise to three additional stresses

$$\sigma'_x = -\rho \overline{u'^2}, \quad \tau'_{yx} = -\rho \overline{u'v'}, \quad \tau'_{xz} = -\rho \overline{u'w'}. \quad (3.18)$$

The total stress tensor due to the turbulent velocity components of the flow are

$$\begin{pmatrix} \sigma'_x & \tau'_{xy} & \tau'_{xz} \\ \tau'_{xy} & \sigma'_y & \tau'_{yz} \\ \tau'_{xz} & \tau'_{yz} & \sigma'_z \end{pmatrix} = -\rho \begin{pmatrix} \overline{u'^2} & \overline{u'v'} & \overline{u'w'} \\ \overline{u'v'} & \overline{v'^2} & \overline{v'w'} \\ \overline{u'w'} & \overline{v'w'} & \overline{w'^2} \end{pmatrix}. \quad (3.19)$$

The presence of fluctuations presents itself as an apparent increase in stresses (viscosity). These additional stresses over the mean or laminar stresses are termed apparent stresses or Reynolds stresses.

## B. TURBULENCE MODELING

The presence of Reynolds stresses in turbulent flow introduces additional unknowns in the Navier-Stokes equations. Therefore, the Navier-Stokes equations, continuity, the perfect gas law, and the energy equation are no longer sufficient to completely define a solution. This is known as the closure problem and is usually resolved by turbulence modeling. [Ref. 17]

A common method used is to relate the turbulent stress to the mean flow properties through empirically based algebraic formulas. An eddy viscosity,  $\nu_t$ , is defined in the same form as the laminar viscosity. Previous models related surface boundary conditions to points in the fluid away from the boundaries through wall functions. This avoided modeling the direct influence of the eddy viscosity; however, it is only applicable in regions where the Reynolds number is high enough for viscous effects to be unimportant or where universal wall functions are well established. In turbulent boundary layers at low Reynolds numbers, in unsteady or in separated flows, or in three-dimensional flows, the flow close to the wall must be described. [Ref. 18]

A common algebraic turbulence model divides the flow into an inner and outer layer. The inner layer is defined by a modified mixing length formula that utilizes some damping function. The outer layer includes the wake and another damping function. [Ref. 17]

Other empirical methods currently in use, such as the  $e^n$  method, predict transition. The  $e^n$  method is a stability method, based on linear stability theory. It assumes transition begins when a small disturbance is introduced at or below a critical Reynolds number. The transition is amplified by  $e^9$ . This method allows greater generality of the flow, however the formulation still relies on empirical terms. [Ref. 19]

The accuracy of turbulence models are limited by the accuracy of the empirical constants. Caution must be taken when using a model under different conditions, i.e., a different flight regime or a radically different airfoil. The turbulence models mentioned above can be fairly simple; a more complex model is still not generally usable because of the computation costs involved and the uncertainty of the constants.

The influence of turbulence and the transition from laminar to turbulent flow on the airfoil need to be understood and accurately modeled for a good description of the flow over the airfoil to be detailed. As experimental methods continue to improve and as computational methods



utilize the data, improvement in the detail of the flow field and in flow prediction will follow.

### 1. Cebeci-Smith Turbulence Models

The turbulence model used in the Cebeci Interactive Boundary Layer (IBL) is a simple algebraic eddy viscosity expression. Simple algebraic models seem to adequately predict turbulent flow for wall boundary layer flows in which the Reynolds shear stress and frequency do not change rapidly. However, if the rate of change of shear stress or the frequency is large, turbulence models are not currently satisfactory. [Ref. 2]

The Cebeci IBL code utilizes the algebraic eddy-viscosity formulation of Cebeci and Smith [Ref. 20]. The turbulent eddy viscosity,  $\nu_t$ , for wall boundary flows is defined by two separate formulas; one for the inner region, based on the Van Driest approach, and the other for the outer region, based on a velocity defect approach:

$$\nu_t = \begin{cases} \{0.4y[1 - \exp(-y/A)]\}^2 \left| \frac{\partial u}{\partial y} \right| \gamma_{tr} & \text{for } 0 \leq y \leq y_C \\ \alpha \int_0^\infty (u_e - u) dy \gamma_{tr} \gamma & \text{for } y_C \leq y \leq \delta \end{cases} \quad (3.20)$$

where:

$$A = 26\nu \left| \left( \nu \frac{\partial u}{\partial y} \right)_{\max} \right|^{1/2} \quad \text{and}$$

$$\gamma = \frac{1}{1 + 5.5(y/\delta)^2}.$$

The continuity of the eddy viscosity defines  $y_c$ ; the expression for the inner region is used outward from the wall until it agrees with the outer region, which is then used.  $\gamma_{tr}$  is an intermittency factor which allows for a transition region when progressing from laminar to turbulent flow. It is given by

$$\gamma_{tr} = 1 - \exp\left[-\frac{u_e^3}{G_{\gamma_{tr}} v^2} R_{x_{tr}}^{-1.34} (x - x_{tr}) \int_{x_{tr}}^x \frac{d\xi}{u_e}\right] \quad (3.21)$$

where the transitional Re number,  $Re_{x_{tr}} = (u_e x / \nu_{tr})$ . The empirical constant  $G_{\gamma_{tr}}$  is dependent on the Reynolds number of the flow. High Reynolds numbers flows indicate  $G_{\gamma_{tr}} = 1200$ , lower Reynolds number flows seem to be better modeled by lower values of  $G_{\gamma_{tr}}$ . [Ref. 12]

The parameter  $\alpha$  in the outer region is given by  $\alpha = 0.0163/F^{2.5}$  where  $F$  is the ratio of the normal stress turbulent energy to the shear stress turbulent energy evaluated at the point of maximum shear stress. This can be expressed as

$$F = \frac{\left( \overline{u'^2} - \overline{v'^2} \right) \partial u / \partial x}{\left( -\overline{u'v'} \partial u / \partial y \right) (-u'v')_{\max}} \quad (3.22)$$

The ratio of the time-averaged quantities are assumed to be a function of  $R_T = \tau_w / (-\overline{u'v'})_{\max}$  which can be represented by

$$\beta = \left\{ \frac{\overline{u'^2} - \overline{v'^2}}{-\overline{u'v'}} \right\}_{(-\overline{u'v'})_{\max}} = \begin{cases} \frac{6}{1+2R_T(2-R_T)} & R_T < 1.0 \\ \frac{2R_T}{1+R_T} & R_T \geq 1.0 \end{cases} \quad (3.23)$$

Thus, the expression for  $\alpha$  is

$$\alpha = \frac{0.0168}{[1 - \beta (\partial u / \partial x) / (\partial u / \partial y)]^{2.5}} \quad [\text{Ref. 2}] \quad (3.24)$$

Note that the value of  $\gamma$  has the effect of reducing the eddy viscosity away from the airfoil surface. This turbulence model does not take into account the wake region, nor is it validated for separated flow.

## 2. Baldwin-Lomax Turbulence Model

The Sankar Navier-Stokes (N-S) code also uses an algebraic eddy viscosity model, the Baldwin-Lomax Turbulence Model [Ref. 21]. It is based on the Cebeci-Smith two layer model [Ref. 22] used in the Cebeci IBL code and may be expressed as

$$v_t = \begin{cases} \{.4y[1 - \exp(-y/A)]\}^2 |\omega| & \text{for } 0 \leq y \leq y_c \\ .0168(1.6) F_{\text{wake}} F_{\text{Kleb}}(y) & \text{for } y_c \leq y \leq \delta \end{cases} \quad (3.25)$$

where

$$A = 26.$$

The inner region is the same mixing length formula of the Cebeci-Smith model, simplified. No intermittancy factor is included (flow is calculated as wholly turbulent),  $A$  is a constant rather than being dependent on viscosity and velocity gradients, and the velocity profile ( $du/dy$ ) is replaced with the product of vorticity and density. [Ref. 13]

The outer region is based on the wake function,  $F_{wake}$  and the Klebanoff intermittancy factor,  $F_{Kleb}(y)$ . [Ref. 23]

$$F_{wake} = \min(y_{max} F_{max}, .25 y_{max} U_{dif}^2 / F_{max}) . \quad (3.26)$$

$$F_{Kleb}(y) = [1 + 5.5 (.3y/y_{max}^6)^{-1}] \quad (3.27)$$

The quantities  $y_{max}$  and  $F_{max}$  are the maximum values obtained from the function

$$F(y) = y |\omega| \{1 - \exp(-y^+/A^+)\} \quad (3.28)$$

which is a form of the mixing length formula used in the inner region.

$U_{dif}$  is the difference between the maximum and minimum velocity of the velocity profile.  $F_{wake}$  is similar to the  $\gamma$  of the Cebeci-Smith turbulence model and thus also reduces eddy viscosity away from the airfoil surface.

This model has been used in separated flows and in the wake, however its validity is not assured in these regions.

#### IV. THE BOUNDARY LAYER EQUATION

Prandtl clarified the influence of viscosity in high Reynolds flows by simplifying the Navier-Stokes equations to yield approximate solutions. He divided the air flow over a body into two regions:

- 1) The region near the surface where viscous forces dominate.
- 2) The rest of the flow where inertia forces dominate; this region may be considered frictionless and potential.

Consider a 2-D incompressible flow over a body. Most of the flow is moving at free stream velocity. However, at the surface the velocity is zero, increasing to free stream at some distance from the surface as shown in Figure 4.1. In this first region, called the boundary layer, the velocity gradient normal to the wall,  $\partial u / \partial y$ , is very large, as is the shearing stress,

$$\tau = \mu \frac{\partial u}{\partial y} \quad (4.1)$$

The two regions are not distinct, but are usually divided at the streamline where the velocity reaches 99% of the free stream velocity.

Simplification of the Navier-Stokes equations will be accomplished by doing an order of magnitude analysis of each term. The following assumptions are made:



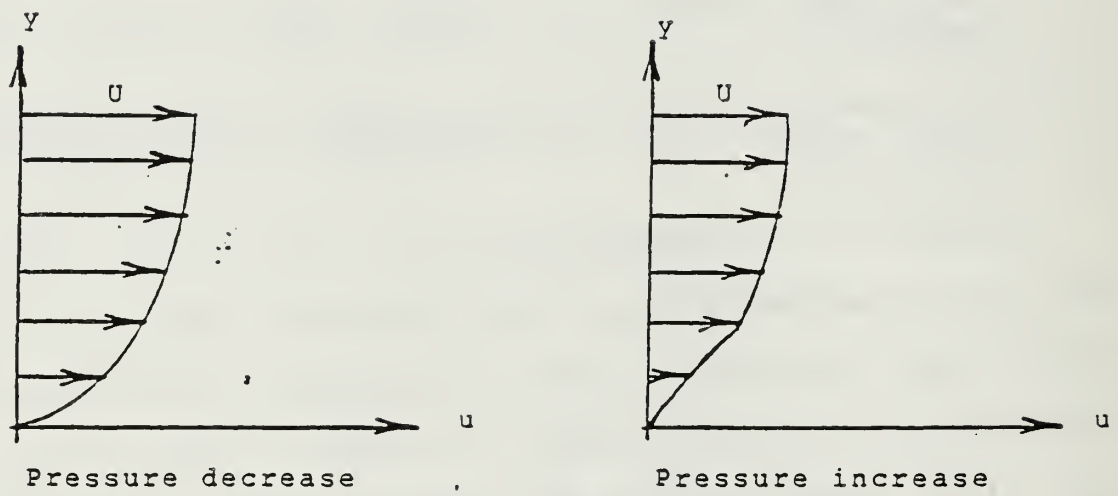


Figure 4.1 Velocity Profile

- 1) A flat wall coinciding with the x-direction, with the y axis perpendicular.
- 2)  $\delta \ll L$   
 $\delta/L \ll 1$

where  $\delta$  is boundary layer thickness and  $L$  is a linear dimension of the body so selected to ensure  $\partial u / \partial x = 1$  under the region in consideration.

- 3) The Reynolds number,  $R = UL\rho / \mu = \frac{UL}{\nu}$  is large. [Ref. 16]

The Navier-Stokes equations are rewritten in dimensionless form:

- Velocities are with respect to the free stream velocity,  $U$ .
- Linear dimensions are with respect to a characteristic length,  $L$ .
- Pressure is divided by  $\rho U^2$ .

Retaining the same symbols for the dimensionless quantities as for their dimensional counterparts, and writing the order of magnitude under each term yields for continuity:

$$\frac{\partial u}{\partial x} + \frac{\partial v}{\partial y} = 0 \quad (4.2)$$

1      1

and for the Navier-Stokes equations:

$$\text{dir } x \quad u \frac{\partial u}{\partial x} + v \frac{\partial u}{\partial y} = - \frac{\partial p}{\partial x} + \frac{1}{R} \left( \frac{\partial^2 u}{\partial x^2} + \frac{\partial^2 u}{\partial y^2} \right) \quad (4.3a)$$

1   1    $\delta$     $\frac{1}{\delta}$                        $\delta^2$    1    $\frac{1}{\delta^2}$

$$\text{dir } y \quad u \frac{\partial v}{\partial x} + v \frac{\partial v}{\partial y} = - \frac{\partial p}{\partial y} + \frac{1}{R} \left( \frac{\partial^2 v}{\partial x^2} + \frac{\partial^2 v}{\partial y^2} \right) \quad (4.3b)$$

1    $\delta$     $\delta$    1                       $\delta$     $\delta^2$     $\delta$     $\frac{1}{\delta}$

At the outer edge of the boundary layer  $u$  equals the steady flow  $U(x)$ . The viscous terms no longer dominate and thus, for the outer flow

$$U \frac{\partial U}{\partial x} = - \frac{1}{\rho} \frac{\partial p}{\partial x} \quad (\text{dimensional}) \quad (4.4)$$

or rewritten in the form of Bernoulli's equation

$$p + \frac{1}{2} \rho U^2 = \text{constant} \quad (4.5)$$

Returning again to dimensional quantities, the simplified Navier-Stokes equations, known as Prandtl's Boundary-Layer Equations may be written:

$$\frac{\partial u}{\partial x} + \frac{\partial v}{\partial y} = 0 \quad (4.6a)$$

$$u \frac{\partial u}{\partial x} + v \frac{\partial u}{\partial y} = - \frac{1}{\rho} \frac{dp}{dx} + \nu \frac{\partial^2 u}{\partial y^2} \quad (4.6b)$$

with the boundary conditions  $y = 0$ :  $u = 0$   $v = 0$ ;  $y = \infty$ :  $u = U(x)$ . Also, a velocity profile at the initial section,  $x = x_0$ , must be prescribed. [Ref. 16]

## V. THE SANKAR NAVIER-STOKES METHOD

The Navier-Stokes Code utilizes the governing equations in conservative form, a body fitted coordinate system, and an Alternating Direction Implicit (ADI) procedure [Ref. 23]. The governing equations in conservative form have the coefficients of the derivative terms constant. The conservative form ensures the conservation of the physical properties.

### A. GRID GENERATION

The requirements of a grid in the physical plane and in the computational plane are conflicting--therefore a grid transformation is advantageous. For ease in computation, equal spacing of grid points is desirable; however, the physical grid needs to be clustered so that the boundary layer and sharply curving surfaces such as the leading edge contain enough points so as to be adequately defined. The boundary conditions must be accurate and should be contained on rectangular surfaces in the computational plane. Also, the grid should be smooth with few discontinuities.

The present code uses an algebraic C-grid which generates a sheared parabolic coordinate system [Ref. 23], first proposed by Jameson [Ref. 24].

First, two points, T and N, are defined on the desired airfoil in the X-Z plane as shown in Figure 5.1. These points are defined by the complex values

$$z_T = x_T + iy_T \quad (5.1a)$$

$$z_N = x_N + iy_N \quad (5.1b)$$

respectively. T is located at the trailing edge of the airfoil and N is located half way between the leading edge and the center of curvature of the leading edge.

Next, the airfoil in the physical plane is transformed as shown in Figure 5.2. A trailing edge vortex sheet shape is assumed to leave the trailing edge smoothly by running tangent to the mean camber line at the trailing edge. The airfoil and wake are then mapped onto the plane by using the following transformation,

$$\zeta = \sqrt{z - z_N} . \quad (5.2)$$

The NACA 0012 airfoil shape transforms to that shown in Figure 5.3. Cubic interpolation defines additional points to smooth the surface.

The far field boundaries are mapped in the physical and computational planes as shown in Figure 5.4.

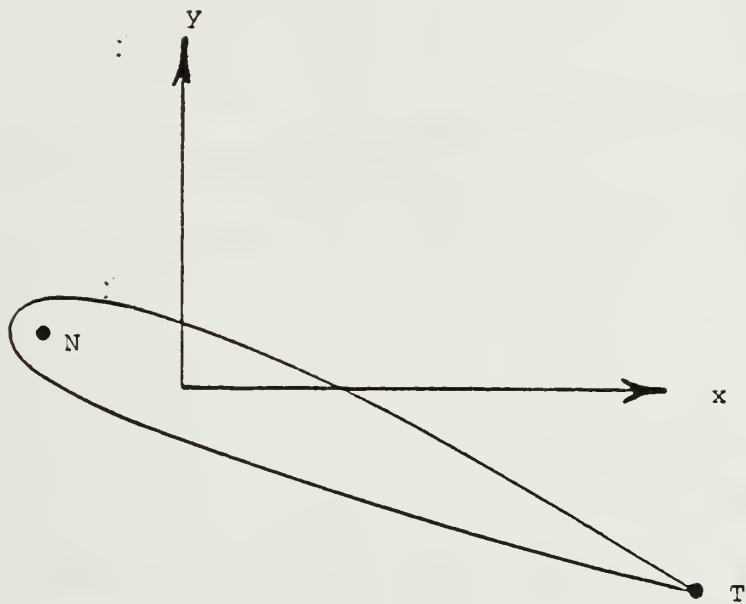
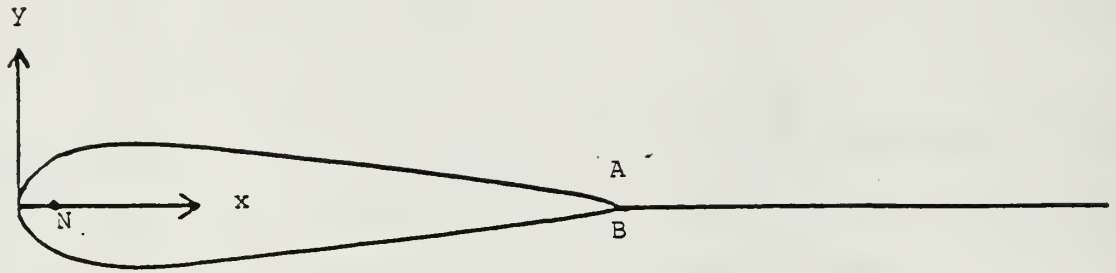


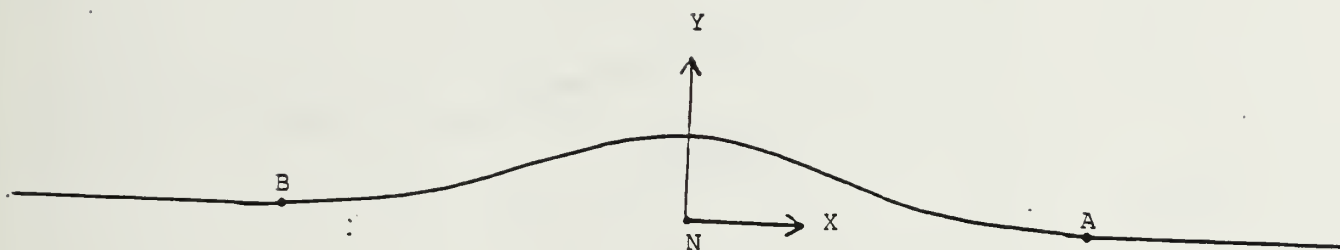
Figure 5.1 Defined Points on the Airfoil Surface





Source: (Ref. 13:p. 19)

Figure 5.2 Symmetric Airfoil in the Physical Plane



Source: (Ref. 13:p. 19)

Figure 5.3 Symmetric Airfoil Unwrapped in  
the Intermediate Plane

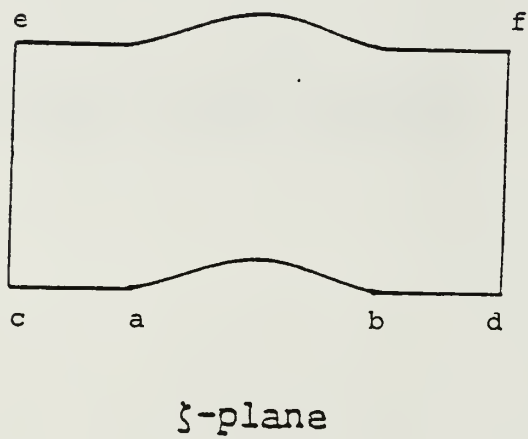
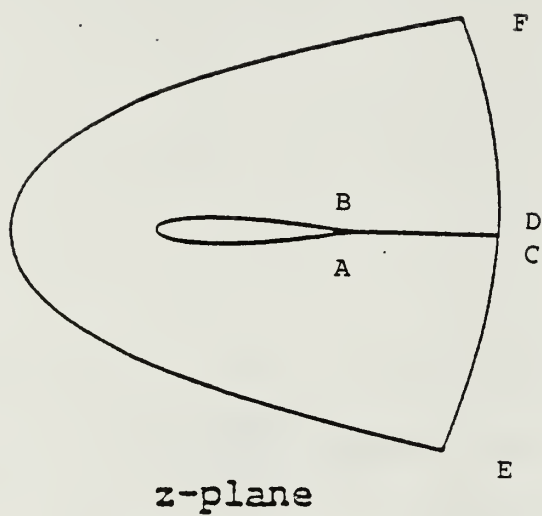


Figure 5.4 Far Field Boundaries

A sheared Cartesian coordinate system is then constructed in the  $\zeta$  plane. It consists of straight vertical lines which then contain specified clustered spacings defined by a stretching function. This allows the grid size to increase normal to the surface.

Lastly, the grid is mapped back to the physical plane. The points on the computational plane,  $\zeta$ , are given by

$$\zeta = \xi + i\eta \quad (5.3)$$

and on the physical plane by

$$x - x_n = \xi^2 + \eta^2 \quad (5.4a)$$

$$y - y_n = 2\xi\eta \quad (5.4b)$$

[Refs. 13,23].

The present method uses a grid containing 161 points in the  $\xi$  direction and 41 points in the  $\eta$  direction. The final grid in the physical plane is shown in Figure 5.5 and a detail of the grid around a NACA 0012 airfoil is presented in Figure 5.6.

## B. INITIAL CONDITIONS AND BOUNDARY CONDITIONS

The initial conditions for viscous flows are the free stream conditions. Viscous dissipation inherent in the equations will minimize errors in this approximation after a sufficient time. Inviscid flows require the proper combination of "artificial" dissipation and boundary conditions for the correct result.

# GRID

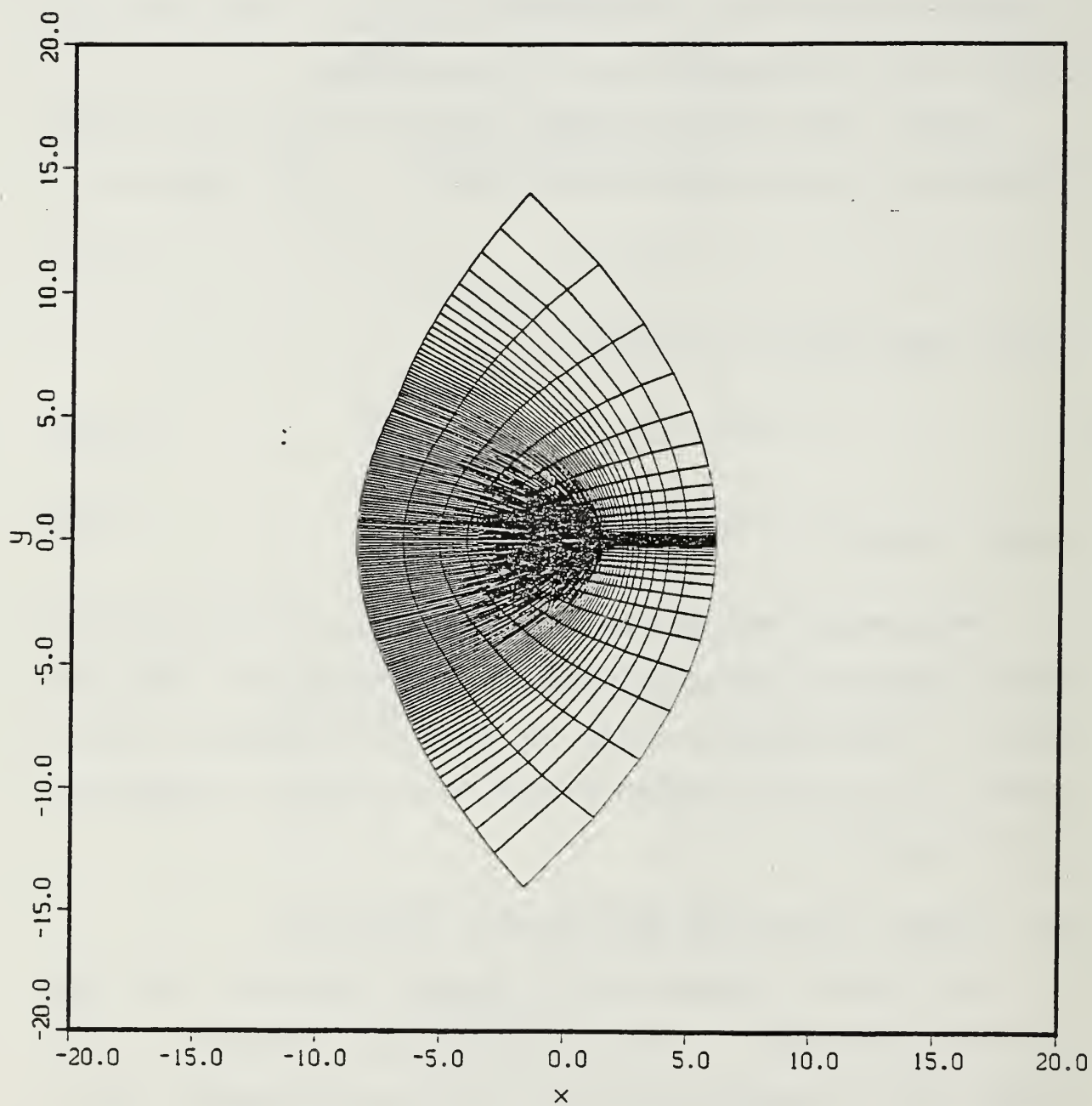


Figure 5.5 Final Grid in the Physical Plane

# GRID

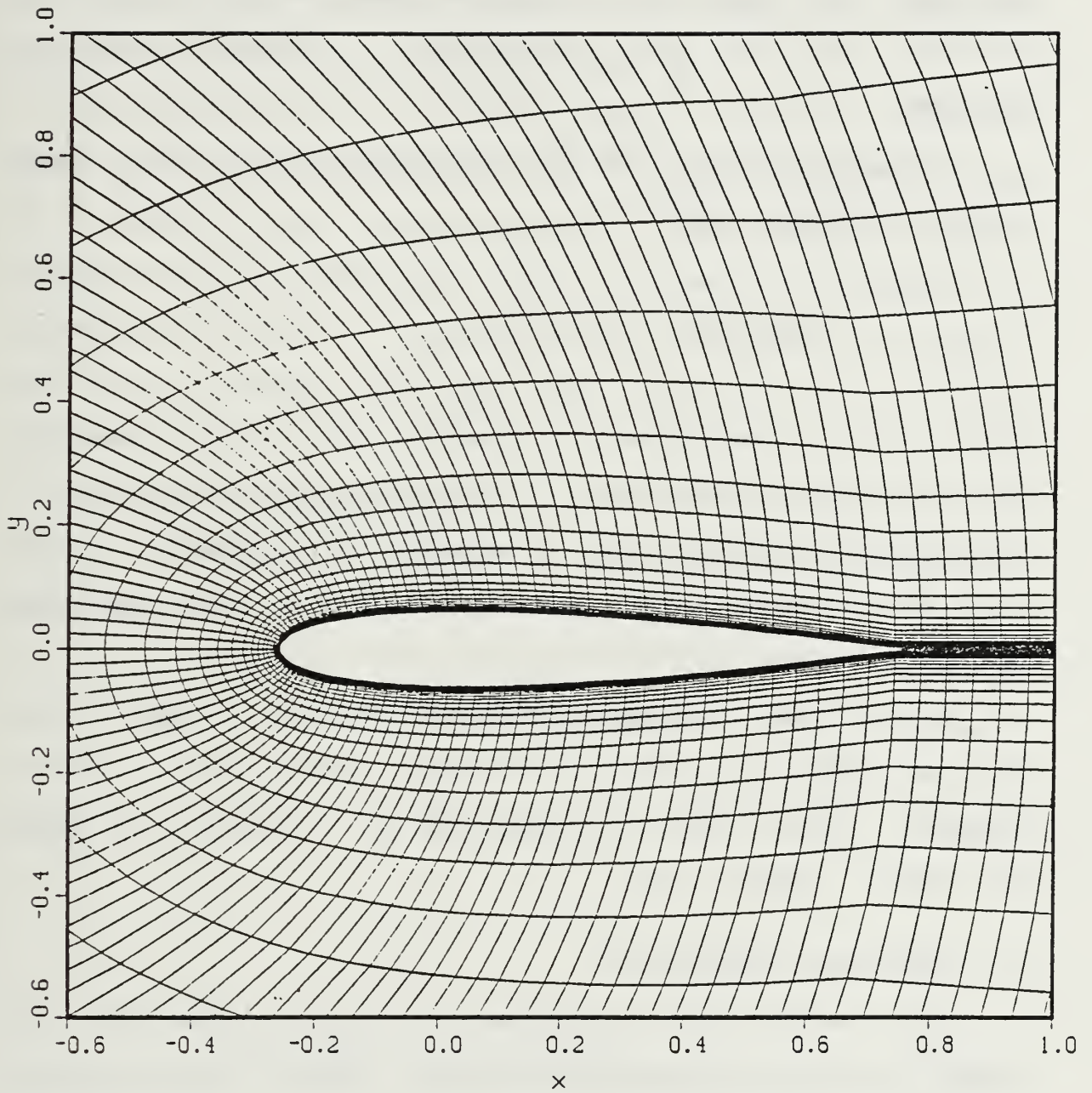


Figure 5.6 Detail of Grid Around the Airfoil



Boundary conditions must be defined on the airfoil, at the far field, and in the wake. On the solid surface, two conditions must be satisfied; no penetration of the surface and the solid and fluid have the same velocity at their boundary (the no slip condition). Adiabatic flow is assumed.

In the far field, the flow is represented by the linear small disturbance equation

$$(1 - M_{\infty})^2 \phi_{xx} + \phi_{yy} = 0 \quad (5.5)$$

where  $\phi$  is the perturbation potential and  $x$  and  $y$  are the physical plane coordinates. This model is used instead of specifying flow conditions at infinity to compensate for the loss of lift experienced when the boundary is not placed far enough away from the solid surface [Ref. 23].

In the wake, the grid procedure produces a "cut" along the coordinate line from the trailing edge to the far field boundary. Here, the flow properties are averaged from above and below. [Refs. 3,13]

### C. NUMERICAL FORMULATION

The coupled and non-linear governing equations are solved using an alternating direction implicit time marching procedure similar to that developed by Beam and Warming [Ref. 4] and as used by Steger [Ref. 5]. The governing equations are assumed to have a solution at some time  $t_n$  and

the solution is then advanced to some time  $t_{n+1}$  using Euler implicit time differencing. The equation is then linearized using Taylor expansion and reduced to a series of one-dimensional problems using the Beam and Warming approximate factorization method [Ref. 5].

The procedure is not fully implicit since the viscous terms are lagged by one time step. Artificial dissipation is included in both second and fourth order terms to obtain accurate surface pressures. The ADI procedure is limited in time step because of accuracy but the explicit boundary conditions further limit the step size due to stability considerations.

### 1. Governing Equations

The governing equation in the computational plane is given as

$$\partial_T \mathbf{q} + \partial_\xi \mathbf{E} + \partial_\eta \mathbf{F} = \text{Re}^{-1} (\partial_\xi \mathbf{R} + \partial_\eta \mathbf{S}) \quad (5.6)$$

where

$$\mathbf{q} = \vec{q}/J \quad (5.7)$$

$$\mathbf{E} = (\xi_t \vec{q} + \xi_x \vec{E} + \xi_y \vec{F})/J \quad (5.8)$$

$$\mathbf{F} = (\eta_t \vec{q} + \eta_x \vec{E} + \eta_y \vec{F})/J \quad (5.9)$$

$$\mathbf{R} = (\xi_{\mathbf{x}} \vec{\mathbf{R}} + \xi_{\mathbf{y}} \vec{\mathbf{S}})/J \quad (5.10)$$

$$\mathbf{S} = (\eta_{\mathbf{x}} \vec{\mathbf{R}} + \eta_{\mathbf{y}} \vec{\mathbf{S}})/J \quad (5.11)$$

$$\tau_{xx} = (\lambda + 2\mu) (\xi_{\mathbf{x}} u_{\xi} + \eta_{\mathbf{x}} u_{\eta}) + \lambda (\xi_{\mathbf{y}} v_{\xi} + \eta_{\mathbf{y}} v_{\eta}) \quad (5.12a)$$

$$\tau_{xy} = \mu [(\xi_{\mathbf{y}} u_{\xi} + \eta_{\mathbf{y}} u_{\eta}) + (\xi_{\mathbf{x}} v_{\xi} + \eta_{\mathbf{x}} v_{\eta})] \quad (5.12b)$$

$$\tau_{yy} = (\lambda + 2\mu) (\xi_{\mathbf{y}} v_{\xi} + \eta_{\mathbf{y}} v_{\eta}) + \lambda (\xi_{\mathbf{x}} u_{\xi} + \eta_{\mathbf{x}} u_{\eta}) \quad (5.12c)$$

$$R_4 = u \tau_{xx} + v \tau_{xy} + kPr^{-1}(\gamma-1) (\xi_{\mathbf{x}} \partial_{\xi} a^2 + \eta_{\mathbf{x}} \partial_{\eta} a^2) \quad (5.13a)$$

$$S_4 = u \tau_{xy} + v \tau_{yy} + kPr^{-1}(\gamma-1) (\xi_{\mathbf{y}} \partial_{\xi} a^2 + \eta_{\mathbf{y}} \partial_{\eta} a^2) \quad (5.13b)$$

J is the transformation Jacobian:

$$J = \xi_{\mathbf{x}} \eta_{\mathbf{y}} - \xi_{\mathbf{y}} \eta_{\mathbf{x}} = (x_{\xi} y_{\eta} - x_{\eta} y_{\xi})^{-1} \quad (5.14)$$

Also,

$$\xi_{\mathbf{x}} = J y_{\eta} \quad (5.15a)$$

$$\xi_{\mathbf{y}} = -J x_{\eta} \quad (5.15b)$$

$$\eta_{\mathbf{x}} = -J y_{\xi} \quad (5.15c)$$

$$\eta_y = Jx_\xi \quad (5.15d)$$

$$\xi_t = -x_\tau \xi_x - y_\tau \xi_y \quad (5.15e)$$

$$\eta_t = -x_\tau \eta_x - y_\tau \eta_y \quad (5.15f)$$

Details of the derivation of the governing equations in the physical plane and transformation of the governing equations to the computational plane are contained in References 13 and 23.

## 2. Time Differencing and Linearization

The governing equations cannot be solved directly in the form of Equation (5.6) because of their non-linearity. This is overcome by writing the flow quantities  $\rho$ ,  $\rho u$ ,  $\rho v$ , and  $e$  at their new time level as their value at the known time level and their increment, i.e.,

$$\rho^{n+1} = \rho^n + \Delta\rho^{n+1} \quad (5.16)$$

The variable  $q$  can therefore be written at the new time level  $t_{n+1}$  as

$$q^{n+1} = q^n + \Delta q^{n+1} \quad (5.17a)$$

or

$$\Delta q^{n+1} = q^{n+1} - q^n . \quad (5.17b)$$

A Taylor series expansion of  $q^n$  backward about  $q^{n+1}$  yields

$$q^n = q^{n+1} - \Delta t \delta_t q^{n+1} + O(\Delta t^2) \quad (5.18a)$$

$$q^{n+1} - q^n = \Delta t \delta_t q^{n+1} + O(\Delta t^2) = \Delta q^{n+1} \quad (5.18b)$$

Using the same procedure with central differencing for the spatial derivatives and substituting into the above equation yields

$$\begin{aligned} \Delta q^{n+1} = -\Delta t (\delta_\xi E^{n+1} + \delta_\eta F^{n+1}) + \Delta R e^{-1} (\delta_\xi R^{n+1} \\ + \delta_\eta S^{n+1}) + O(\Delta t^2) \end{aligned} \quad (5.19)$$

where  $\delta_\xi$  and  $\delta_\eta$  are second order accurate difference operators.

Backward differencing is first order accurate and central differencing is second order accurate, therefore the Equation (5.19) is first order accurate in time and second order accurate in space.

The governing equation, Equation (5.6), is still non-linear. So that it can be solved directly rather than iteratively, it is linearized. First E and F are rewritten using a local Taylor expansion at  $q^n$ :

$$\mathbf{E}^{n+1} = \mathbf{E}^n + [\partial \mathbf{qE}]^n \Delta \mathbf{q}^{n+1} + o(\Delta t^2) \quad (5.20a)$$

$$\mathbf{F}^{n+1} = \mathbf{F}^n + [\partial \mathbf{qF}]^n \Delta \mathbf{q}^{n+1} + o(\Delta t^2) \quad (5.20b)$$

where  $[\partial \mathbf{qE}]$  and  $[\partial \mathbf{qF}]$  are Jacobian matrices. [Ref. 23]  
Substituting Equation (5.20) into the time differenced governing equation, Equation (5.19), yields

$$\begin{aligned} & ([\mathbf{I}] + \Delta t \delta_{\xi} [\partial \mathbf{qE}]^n + \Delta t \delta_{\eta} [\partial \mathbf{qF}]^n) \{\Delta \mathbf{q}\}^{n+1} \\ &= -\Delta t (\delta_{\xi} \mathbf{E}^n + \delta_{\eta} \mathbf{F}^n) + \Delta t \mathbf{Re}^{-1} (\delta_{\xi} \mathbf{R}^{n+1} + \delta_{\eta} \mathbf{S}^{n+1}) \end{aligned} \quad (5.21)$$

This can be expressed as

$$([\mathbf{I}] + \Delta t \delta_{\xi} [\mathbf{A}] + \Delta t \delta_{\eta} [\mathbf{B}]) \{\Delta \mathbf{q}\}^{n+1} = \{\mathbf{R}\}^n \quad (5.22)$$

where:

$$[\mathbf{A}] = [\partial \mathbf{qE}]^n \quad (5.23)$$

$$[\mathbf{B}] = \{\partial \mathbf{qF}\}^n \quad (5.24)$$

$$\{\mathbf{R}\}^n = -\Delta t (\delta_{\xi} \mathbf{E}^n + \delta_{\eta} \mathbf{F}^n) + \Delta t \mathbf{Re}^{-1} (\delta_{\xi} \mathbf{R}^{n+1} + \delta_{\eta} \mathbf{S}^{n+1}) \quad (5.25)$$

The governing equations for the unknown vector  $\{\Delta \mathbf{q}\}^{n+1}$  are now linear and may be solved numerically.



### 3. The Alternating Direction Implicit Procedure

An approximation factorization method, developed by Beam and Warming [Ref. 4] is now used to solve the governing equation Equation (5.22), which has been linearized in  $[\Delta q]^{n+1}$ . Although Equation (5.22) could be solved directly, Beam and Warming's method reduces the large (and thus costly) matrix into a sequence of one-dimensional problems.

The governing equation is approximated as

$$([I] + \Delta t \delta_{\xi}[A])([I] + \Delta t \delta_{\eta}[B])\{\Delta q\}^{n+1} = \{R\}^n \quad (5.26)$$

which is then rewritten as two equations

$$([I] + \Delta t \delta_{\xi}[A])\{\Delta q^*\} = \{R\}^n \quad (5.27a)$$

$$([I] + \Delta t \delta_{\eta}[B])\{\Delta q\}^{n+1} = \{\Delta q^*\} \quad (5.27b)$$

Since  $\delta_{\xi}$  and  $\delta_{\eta}$  are central difference operators, Equations (5.27) are systems of block tridiagonal matrix equations composed of 4x4 submatrices. These can be solved by one of several methods, such as LU decomposition. Once  $\{\Delta q\}^{n+1}$  is obtained,  $\{q\}^{n+1}$  can also be obtained from

$$\{q\}^{n+1} = \{q\}^n + \{\Delta q\}^{n+1} \quad (5.28)$$

Boundary conditions at  $\{\Delta q\}$  as well as the defined vector  $\{\Delta q^*\}$  must be defined.

#### 4. Stability and Accuracy Considerations

The ADI approach is implicit with explicit boundary conditions and viscous terms that are lagged by one time step. Implicit numerical methods theoretically are unconditionally stable with the size of the time step limited by accuracy rather than stability. The time step stability limit imposed by the explicit boundary conditions must therefore be less than the accuracy time step limit. [Ref. 4]

A linear stability analysis for an explicit procedure is performed [Ref. 23] to determine the maximum time step possible, then a very conservative estimate is used. When calculating steady-state flow, the convergence of the calculations can be improved by introducing a variable time step. This allows small time steps where the grid must be highly clustered, such as the boundary layer, in regions of shocks, and near stagnation points, and large time steps elsewhere where the grid is larger. [Ref. 23]

Viscosity slows a flow down by dissipating energy. Mathematically, this results in a reduction of flow field gradients. The mathematical formulations used to include viscosity in a flow can therefore also be applied to suppress errors inherently generated in certain methods. [Ref. 25]

The capability of including this "artificial viscosity" as used by Murman and Cole [Ref. 26] is implemented through backward differencing in a Taylor series expansion. The truncation term mimics viscosity and is known as artificial viscosity. When the method includes this dissipative term it is known as implicit artificial viscosity. Often however, more dissipation is required for convergence or stability, or because it is advantageous to apply selective dissipation. Then, explicit artificial viscosity or explicit dissipation is included in the numerical formulation.

Central differencing in a Taylor series expansion decouples the even from the odd terms, causing high frequency errors. The spatial derivatives are formulated through central differencing and thus contain these errors which influence the solution accuracy when using large time steps. The time derivatives are formulated through backward differencing; their artificial viscosity terms and the viscous terms suppress this error somewhat. To further dissipate the high frequency errors, especially in high Reynolds number and inviscid flows, both fourth order and second order artificial dissipation is explicitly applied to the right hand side of the discretized governing equations as was done by Jameson [Ref. 24]. [Ref. 23]

The fourth order terms alone lead to overshoots in the vicinity of shocks. The second order dissipative terms

correct this but tend to smear results in regions such as the leading edge. This is resolved by implementing second order dissipation only in regions of high pressure gradients. Including artificial dissipation in the right hand side of Equation (5.26) also corrects for incorrect initial conditions after a sufficient time step.

To allow the viscous terms to be explicitly modulated and to remove any explicit stability limits, artificial dissipation is also implicitly included in the left hand side of Equation (5.26). The inclusion of explicit and implicit artificial dissipation yields [Ref. 23]

$$\begin{aligned}
 & ([I] + \Delta t \delta_{\xi} [A] - \xi_I J^{-1} \delta_{\xi\xi} J) ([I] + \Delta t \delta_{\eta} [B] - \xi_1 J^{-1} \delta_{\eta\eta} J) (\Delta q)^{n+1} \\
 & = \{R\}^{n+1} - (D_i - D_{i-1}) - J^{-1} \delta_{\eta\eta\eta\eta} (Jq) \quad (5.29)
 \end{aligned}$$

where  $\xi$  is a function of the maximum pressure gradient and  $D$  and  $D_{i-1}$  are either second or fourth order dissipation. The artificial dissipation terms do not affect the accuracy of the formulation since all terms are of the same order as or smaller than the truncation errors associated with the spatial and time difference formulas.

## 5. Application of Boundary Conditions

All of the boundary conditions are explicitly applied after the ADI sweeps at each time step. The explicit method was used because of its ease of implementation in the code even though implicit boundary conditions are more desirable because of accuracy and stability considerations. [Ref. 23]

On the airfoil surface the no-slip condition and the assumption of no flow through the surface correspond to

$$\partial p / \partial \eta = 0 \qquad \partial \rho / \partial \eta = 0 \qquad (5.30)$$

Adiabatic flow is assumed. A two point extrapolation of the above yield  $p$  and  $\rho$  to be [Ref. 14]

$$P_{i,1} = (4P_{i,2} - P_{i,3})/3 \qquad (5.31a)$$

$$\rho_{i,1} = (4\rho_{i,2} - \rho_{i,3})/3 \qquad (5.31b)$$

Internal energy and the coefficient of pressure may be obtained from the calculation of  $p$  and  $\rho$ . The incremental quantities  $\{\Delta q^*\}$  and  $\{\Delta q\}^{n+1}$  are also assumed zero on the solid surface and are solved in a similar manner as for  $p$  and  $\rho$ . The far field boundary conditions are assumed to be free stream plus the disturbances caused by the far field



not being placed at infinity as described in Section V.B. Internal energy is evaluated from

$$\epsilon = \frac{p}{\gamma-1} + .5\rho(u^2 + v^2) \quad (5.32)$$

The downstream boundary conditions are extrapolated from the adjacent interior points. At the boundary, pressure is taken to be freestream.

The cut inherent in the grid system divides the flow above and below the line emanating from the trailing edge. The flow quantities on the cut are obtained by averaging the values of the interior points above and below the cut. This is acceptable because of the denseness of the grid in this region. [Ref. 23]

#### D. USE OF SANKAR'S N-S CODE

Reference 13 details the use of Sankar's N-S code for both steady and unsteady flows. The code is submitted to the NASA X-MP Cray via Job Control Cards. JCL options are selected so to access files where output data is stored or to send data to a specific directory. Job Cards also provide account and time limit information.

The main program contains all of the "Write" statements, which may or may not be required. Output information includes input data, airfoil coordinates in the physical and computational planes, grid information, residuals, pressure and skin friction profiles, coefficients of lift, drag and



moment, and velocity profile information. The time step intervals at which these are printed is specified within the program.

The majority of the program inputs are located in data cards. These inputs and their definitions are described in Table 5.1. See Reference 13 for a detailed program description. The values used when implementing the Sankar N-S code are given in Table 5.2.

TABLE 5.1

## INPUT PARAMETERS FOR THE SANKAR N-S CODE

<u>INPUT</u>	<u>DESCRIPTION</u>
IMAX	Number of x coordinate locations
KMAX	Number of y coordinate locations
DT	Size of time step
WW	Explicit artificial viscosity term
ALFA	Mean angle of attack
ALFA1	Amplitude of oscillation
ALFAI	Angle below which modified turbulence model is used
REDFRE	Reduced frequency
AMINF	Mach number
FNSTP	Number of time steps
REYREF	Reynolds number in millions
DNMIN	Distance of first point off of the wall
TSTART	Time calculation flag
FULOUT	Plotting file flag
RSTRT	If set, stored values are read to continue iteration
PITCH	Set for dynamic stall, indicates change in AOA
PLUNGE	Set for up and down motion of airfoil
FNU	Number of upper airfoil coordinates
FNL	Number of lower airfoil coordinates
ZSYN	Flag for symmetric airfoil
XP	X airfoil coordinates
YP	Y airfoil coordinates

TABLE 5.2

## VALUES USED FOR SANKAR STEADY N-S CODE

<u>INPUT</u>	<u>VALUE</u>
IMAX	157
KMAX	41
DT	1.00
WW	10-12
ALFA	0-12
ALFA1	0
ALFAI	0
REDFRE	0.0
AMINF	.12, .30
FNSTP	2000-8000
REYREF	1-15
DNMIN	.000005-.0001
TSTART	0
RSTRT	0
PITCH	FALSE
PLUNGE	FALSE
FNU	33
FNL	33
ZSYN	0
XP	X airfoil coordinates for NACA 0012 airfoil
YP	Y airfoil coordinates for NACA 0012 airfoil

## VI. THE CEBECI INTERACTIVE BOUNDARY LAYER METHOD

The Cebeci Interactive Boundary Layer (IBL) code uses a two layer approach; an outer inviscid layer and a viscous inner boundary layer. In this it follows Prandtl's boundary layer theory by assuming the inner viscous flow is the only region where viscous effects are important. The remaining outer region is dominated by inertia terms and can be assumed inviscid. The inviscid outer flow characteristics are determined through Hess and Smith's panel method. The flow is assumed to have a vortex and source distribution such that it gives correct circulation and velocity over the airfoil. The airfoil surface is replaced by a distribution of panels that satisfies the Kutta condition.

The inner viscous flow utilizes the boundary layer method to determine the flow characteristics. A direct boundary layer method is used in regions of large viscous stresses such as near the leading edge. This method prescribes an external velocity and requires the no slip condition to be satisfied. In the rest of the flow, an interactive boundary layer method is used. Here, the edge boundary conditions prescribe a combination of displacement thickness and external velocity. An iterative technique is used to solve for this flow. [Ref. 27]

The inner and outer flow are coupled through an interaction model. The boundary location and velocity are unknown and are solved simultaneously through an iteration between the inner and outer flow equations.

Cebeci's IBL code calculates where transition from laminar to turbulent flow occurs and incorporates a smoothing function. It also predicts separation and allows laminar separation and then transition to turbulent flow and subsequent reattachment of the turbulent flow.

#### A. VISCOUS INNER FLOW

##### 1. Direct Boundary Layer Method

The direct boundary layer method can be used in regions of the boundary layer where the viscous effects have not yet strongly influenced the flow. This usually implies the stagnation point and the airfoil leading edge. The advantage of minimal viscosity influence is the capability of defining a stream function,  $\psi$ , that satisfies the continuity equation

$$u = \partial\psi/\partial y \quad \text{and} \quad v = - \partial\psi/\partial x \quad (6.1)$$

The momentum equation is subjected to the Falknar-Skan transformation [Ref. 2]

$$\eta = \sqrt{\frac{u_e}{\nu x}} y \quad (6.2a)$$

$$f(x, \eta) = \frac{1}{\sqrt{u_e} \sqrt{x}} \psi(x, y) \quad (6.2b)$$

The normal coordinate  $y$  and the stream function  $\psi$  are scaled with respect to the external velocity for convenience and accuracy. The boundary conditions of no flow penetration through the wall and no slip condition at the wall are also transformed. The resulting momentum equation and boundary conditions are given as

$$(bf'')' + \frac{1}{2}(m+1)ff'' + m[1-(f')^2] = x(f' \frac{\partial f'}{\partial x} - f'' \frac{\partial f}{\partial x}) \quad (6.3)$$

where:

$$b = 1 + v_t/v$$

$$m = (x/u_e) (du_e/dx)$$

and

$$\eta = 0: \quad f'(x, 0) = 0, \quad f(x, 0) = 0$$

$$\eta = \eta_e: \quad f'(x, \eta_e) = 1$$

Primes denote differentiation with respect to  $\eta$ . This is a third order partial differential equation and cannot be solved directly. Therefore, the box method developed by Keller [Ref. 28] is used. [Refs. 12,30]



The box method reduces the governing equations to a first order system through introduction of two dependent variables. The flow properties are then evaluated only discretely by defining the solution domain as a rectangular mesh. Instead of solving continuous functions, all parameters are approximated in terms of nodal values and their location on the mesh. The domain of dependence is substantially reduced and the overall solution scheme simplified by solving for the nodal values through central differencing.

The resulting nonlinear system is solved by Newton's method. This iterative procedure linearizes the variables at location  $i$  by rewriting the value at  $i$  as a sum of the value at location  $i-1$  plus some incremental value. Substituting into the governing system of equations results in a linear system of the unknown incremental values which are repeatedly solved until they are small enough to be neglected.

## 2. Interactive Boundary Layer Method

Most of the airfoil is influenced by viscosity, thus the direct boundary layer method can no longer be used. Instead, an interactive boundary layer method is used. It is effective even in regions of rapid flow acceleration, boundary layer separation, and zero skin friction. Both the boundary layer displacement thickness and the external velocity are now unknown. The Mechul function method is

used to solve the flow under these conditions by writing the edge boundary condition as a sum of the inviscid velocity distribution and the perturbation velocity due to viscous effects. The perturbation velocity,  $\delta u_e(x)$ , is determined from the Hilbert integral [Refs. 12,27]

$$\delta u_e(x) = \frac{1}{\pi} \int_{x_a}^{x_b} \frac{d}{d\sigma} (u_e \delta^*) \frac{d\sigma}{x-\sigma} \quad (6.4)$$

where:

$$\frac{d(u_e \delta^*)}{d\sigma} \text{ is the blowing velocity.}$$

The solution method follows the direct boundary layer method with several exceptions. The Falknar-Skan transformation, with its constant boundary layer thickness, is no longer applicable; nor is using  $u_e$  as a reference velocity since  $u_e$  is now unknown. Instead,

$$\eta = \sqrt{\frac{u_o}{\nu x}} y \quad (6.5a)$$

$$f(x,\eta) = \frac{1}{\sqrt{u_o \nu x}} \psi(x,y) \quad (6.5b)$$

where the reference velocity is now taken as  $u_o$ , the free stream velocity. The solution is again a downstream marching technique. The FLARE (Flugge-Lötz and Reyhner) approximation is used to continue the integration through regions of backflow. In these regions, where the velocity

in relation to the forward velocities is assumed small, the streamwise convection term  $u \partial u / \partial x$  is set equal to zero.

### 3. Transition Model

For the IBL technique to be successful, the displacement thickness must be accurately determined. This is dependent on an accurate solution of the laminar and turbulent flow equations, the transition region between them, and when applicable, separated flows.

The values of flow parameters associated with laminar and turbulent flow differ greatly: the boundary layer thickness, momentum thickness, skin friction, velocity profile, and drag are all influenced by increased turbulence. For a code to accurately model the boundary layer flow, both regimes must be modeled as well as the transition between the two and separated flow. The influence of the transition location and length of transition on the accuracy of the solution, especially for low Reynolds flows, has been demonstrated by Reference 12.

The Cebeci IBL code uses Michel's criterion to predict onset of transition. Michel begins transition when the local Reynolds number based on the momentum thickness,  $R_\theta$ , is related to the length Reynolds number by the empirical equation

$$Re = 1.174 \left( 1 + \frac{22.400}{R_x} \right) R_x^{0.46} \quad (6.6)$$

where:

$$R_{\theta} = u_e \theta / \nu ; \text{ and}$$

$$R_x = u_e x / \nu .$$

The transition model is also highly empirical and is as previously given in Equation (3.20).

As implied by the above discussion, turbulence onset and its generation mechanisms are not thoroughly understood. Nonetheless, it is evident that numerical methods need to include transition capabilities to begin to accurately model the boundary layer flow.

#### B. INVISCID OUTER FLOW

Hess and Smith developed a panel method where the flow is represented by a series of vortices and sources. [Ref. 30] They assume the vortex strength to be constant and distributed over the surface such that the correct circulation results. The velocity field is then modeled through a source distribution that forces the velocity to be everywhere tangent to the surface (the no penetration condition). This method is simplified by defining nodes on the airfoil surface and connecting them with straight line panels. Obviously, greater accuracy is achieved by increasing the number of panels on the airfoil. [Ref. 12]

The Kutta condition must also be satisfied. The Kutta condition insures a unique solution by imposing zero loading in the region of the trailing edge. The three basic

principles of the Kutta condition are that the circulation about the airfoil is such that the flow leaves the trailing edge smoothly, the trailing edge is a stagnation point if the trailing edge is finite, and the upper and lower trailing edge velocities are finite and equal if the trailing edge is cusped. The vortex strength is determined from the Kutta condition and the source strength can then be calculated from the vortex strength. [Ref. 30]

### C. STRONG INTERACTION MODEL

The inner and outer flow influence each other and thus cannot be solved separately if viscosity effects on pressure are large. The strong interaction model couples the boundary layer and the external viscous flow by allowing both the displacement thickness and the pressure (which is a function of external velocity) to be unknown. An iterative simultaneous solution is then achieved by alternating between the viscous and inviscid flow equations until convergence is achieved.

The solution method is based on conformal mapping and Fourier analysis techniques [Ref. 31]. The airfoil is mapped onto a circle through a series of conformal mappings and application of the fast Fourier-transform algorithm. It then is mapped onto another circle that includes the boundary layer and so models the inviscid portion of the flow as that over an airfoil whose boundaries have been displaced by the viscous boundary layer. At the surface of



the circle, the no penetration condition does not apply. To account for this, a nonzero normal velocity (blowing velocity) is prescribed. [Ref. 29]

The boundary layer is solved from the surface to the outer boundary. The outer boundary conditions are defined by the interaction law

$$(u_e)^{i,k} = (u_e)^{i,k-1} + \sum_{k=1}^K C_{ik} [(u_e \delta^*)^{k,K-1} (u_e \delta^*)^{k,K-1} \quad (6.7)$$

The solution of this is an approximation that requires several sweeps over the upper and lower surfaces to achieve convergence.

Convergence between the boundary of the two methods is checked and the procedure is repeated by updating the product of the external velocity and displacement thickness until desired convergence is achieved.

#### D. USE OF CEBECI'S IBL CODE

Reference 29 details the use of the Cebeci IBL code. The code is submitted to the Naval Postgraduate School IBM mainframe via Job Control Cards where account information, running time, and size commands are set.

Output information includes input data, coefficients of lift and drag, airfoil coordinates, shear stress, skin friction, displacement and momentum thickness, and velocity profile information. The inputs to the program are located in data cards and are defined in Table 6.1. See Reference



29 for a detailed program description. An example of input parameters used is given in Table 6.2.

TABLE 6.1

## INPUT PARAMETERS FOR THE CEBECI IBL CODE

<u>INPUT</u>	<u>DESCRIPTION</u>
IPT(1)	Flag for specification of lower surface transition
IPT(2)	Flag for specification of upper surface transition
IRSTRT	Flag for restarting solution
IGLMAX	Number of sweeps
IPRINT	Flag for output printed
RL	Reynolds number in millions
XTRL	Lower surface specified transition
XTRU	Upper surface specified transition
ALPO	Angle of attack
GTR	Empirical constant for length of transition
MPTS	Number of coordinates
XP	X airfoil coordinates
YP	Y airfoil coordinates

TABLE 6.2  
VALUES USED FOR THE CEBECI IBL CODE

<u>INPUT</u>	<u>VALUE</u>
IPT(1)	4
IPT(2)	1
IRSTRT	0
IGLMAX	16
IPRINT	2
RL	1-15
XTRL	0
XTRU	.005
ALPO	0-12
GTR	1200
MPTS	101
XP	X airfoil coordinates
YP	Y airfoil coordinates

## VII. PRESENTATION OF COMPUTATIONS

Simulations of steady flow at Reynolds numbers ranging from 1 million to 15 million at zero degrees angle of attack, angle of attack studies for Reynolds numbers of 1.5 million and 6 million all over a NACA 0012 airfoil are presented in this chapter.

Four aerodynamic factors are investigated: coefficient of lift, coefficient of pressure, velocity profiles at specified locations along the chord of the airfoil, and skin friction along the airfoil chord. In the steady flow cases results from the Sankar N-S code are compared with results from the Cebeci IBL code. Numerous studies have documented the validity of the Cebeci code in steady flow [Refs. 2,12, 28,30], however, the Cebeci IBL code only considers incompressible flow. Therefore, the Sankar N-S code was limited to the upper regions of what is normally considered incompressible flow, .3 Mach. Unless otherwise indicated, all cases are run at .3 Mach.

The coefficient of lift as a function of angle of attack is plotted in Figure 7.1 for a NACA 0012 airfoil at a Reynolds number of 6 million. Figure 7.2 shows lift coefficients versus angle of attack for a Reynolds number of 1.5 million.

# LIFT COEFFICIENT

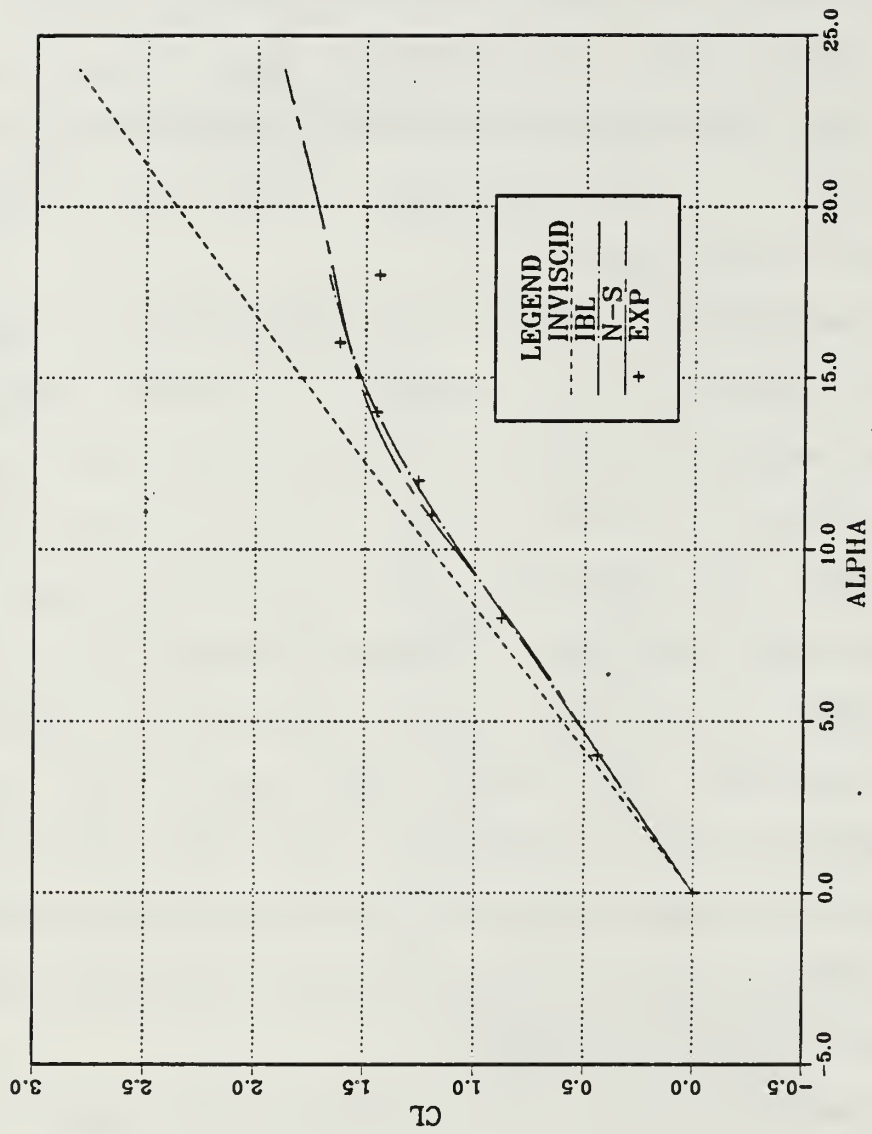


Figure 7-1  $C_L$  vs AOA;  $Re = 6M$ ,  $N-S M = .3$

# LIFT COEFFICIENT

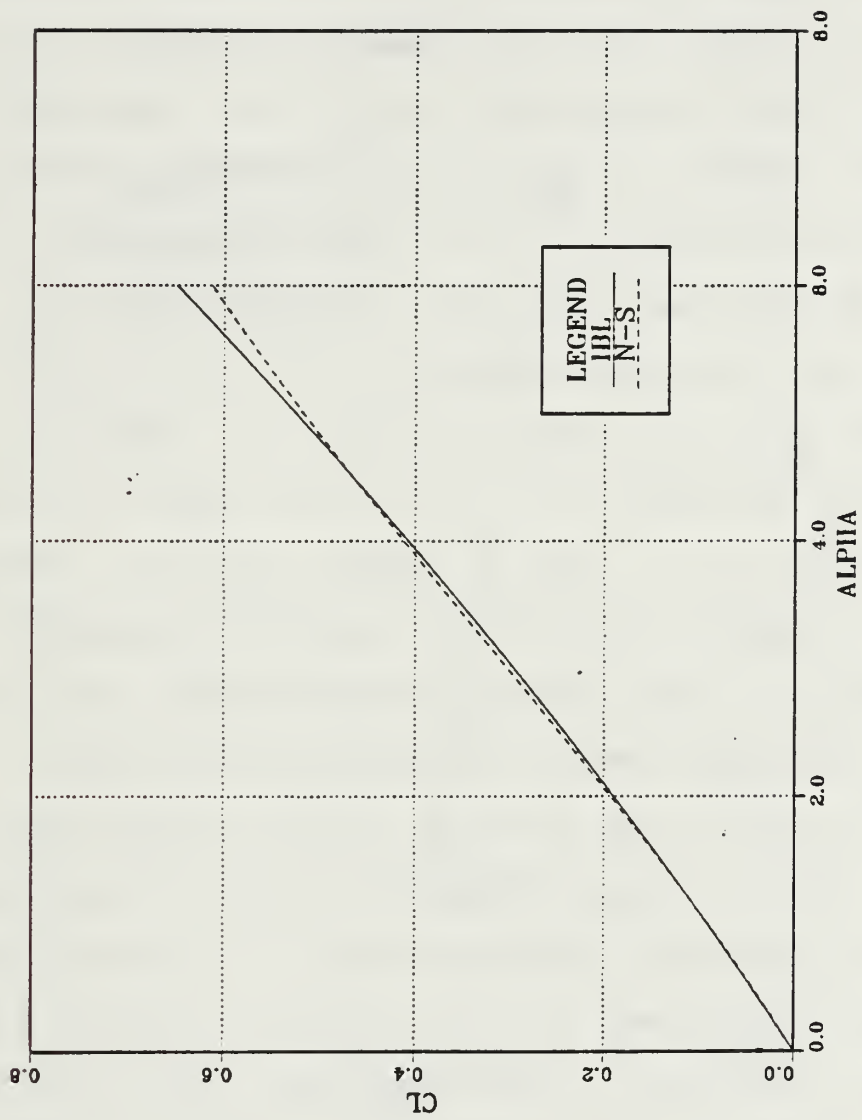


Figure 7.2  $C_L$  vs AOA;  $Re = 1.5M$ , N-S  $M = .12$



Next, the correlation between the suction pressure coefficients for various Reynolds numbers and angles of attack were investigated. At zero degrees angle of attack the coefficient of pressure,  $C_p$ , of the upper surface is the same for the five Reynolds numbers presented: 1, 3, 6, 10, and 15 million, using both Cebeci's IBL code and Sankar's N-S code. Figure 7.3 plots this. Coefficients of pressure at angles of attack of 0, 4, 8, and 12 degrees at a Reynolds number of 6 million and angles of attack of 0, 2, 4, and 6 degrees for a Reynolds number of 1.5 million and a Mach of .12 are shown in Figures 7.4 and 7.5 respectively. The conditions of Figure 7.5; 1.5 million Reynolds number, .12 Mach, and 0, 2, 4, and 6 degrees angle of attack, were chosen to verify steady state conditions presented in Tang [Ref. 23]. The pressure coefficients were compared, however, no other results were presented by Tang.

Skin friction and velocity profile information was then sought. The verification studies done by References 3, 7, 14, and 15 did not address either. Therefore, the only comparisons made were with the Cebeci IBL code. Figure 7.6 shows the coefficient of skin friction,  $C_f$ , as a function of airfoil chord. The Sankar N-S code is calculated as turbulent over the entire airfoil [Ref. 13]. The Cebeci IBL code allows specification of transition from laminar to

# UPPER PRESSURE COEFFICIENT

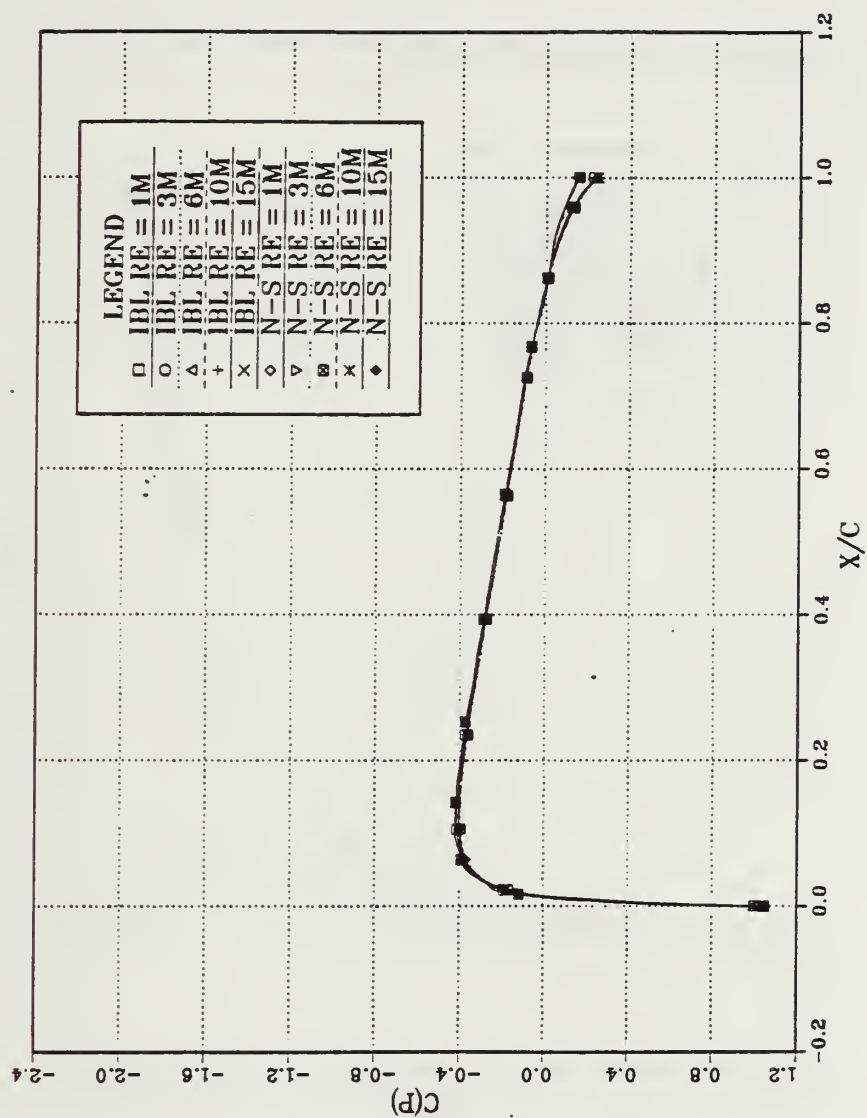


Figure 7.3  $C_p$  vs  $x/c$ ; AOA = 0, N-S M = .3

# UPPER PRESSURE COEFFICIENT

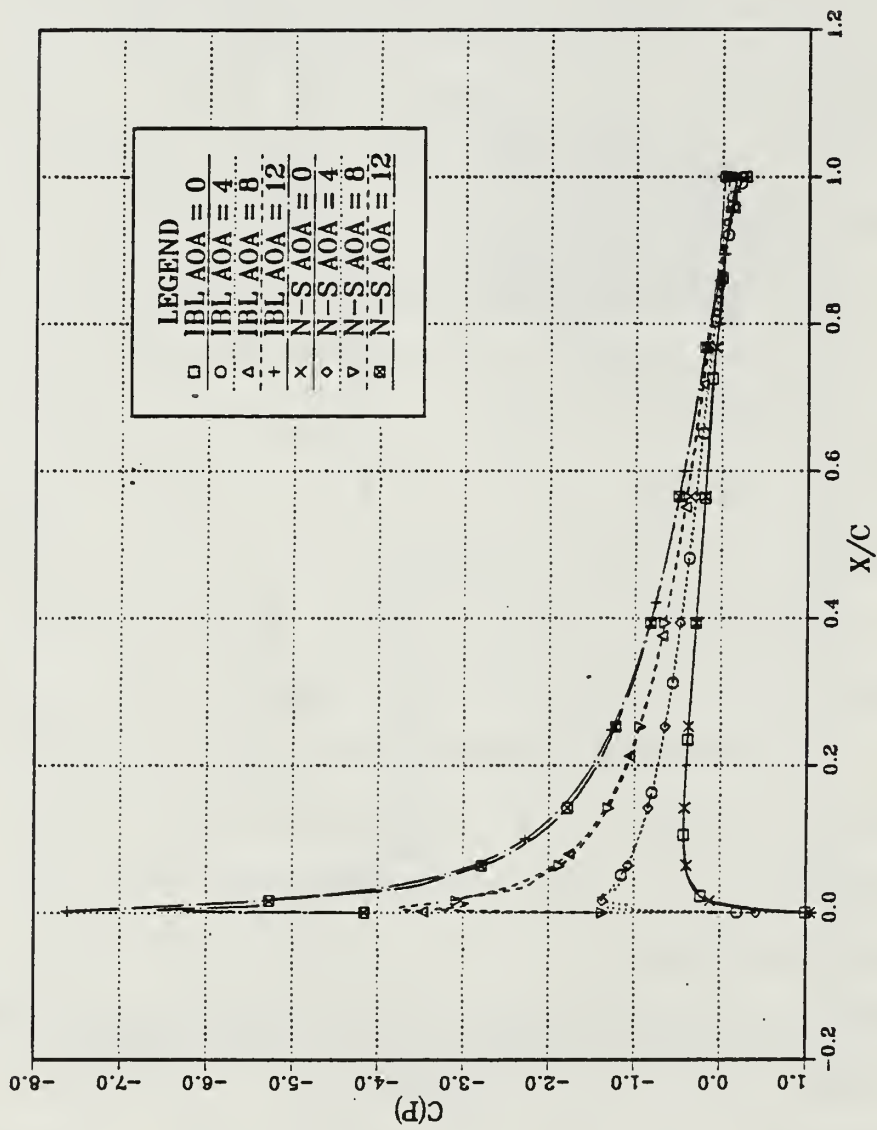


Figure 7.4  $C_p$  vs  $x/c$ ;  $Re = 6M$ ,  $N-S M = .3$

# UPPER PRESSURE COEFFICIENT

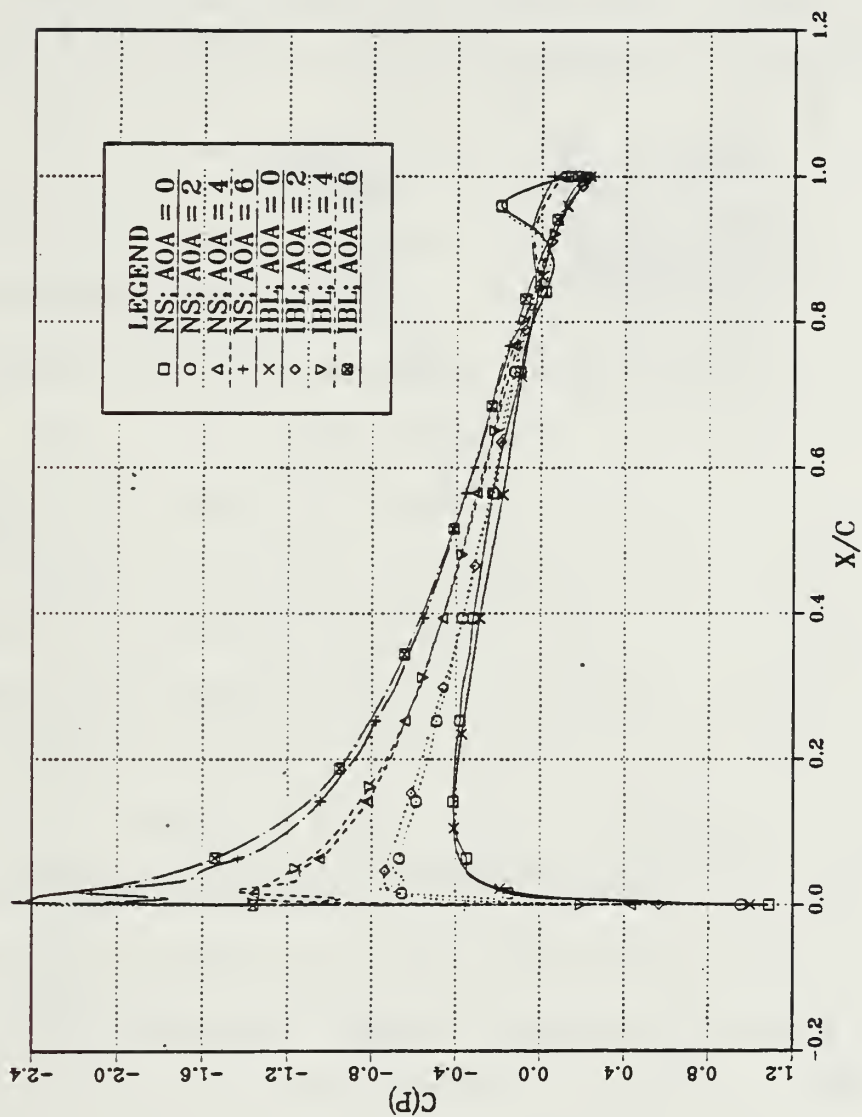


Figure 7.5  $C_p$  vs  $x/c$ ;  $Re = 1.5M$ ,  $N-S M = .12$

# SKIN FRICTION

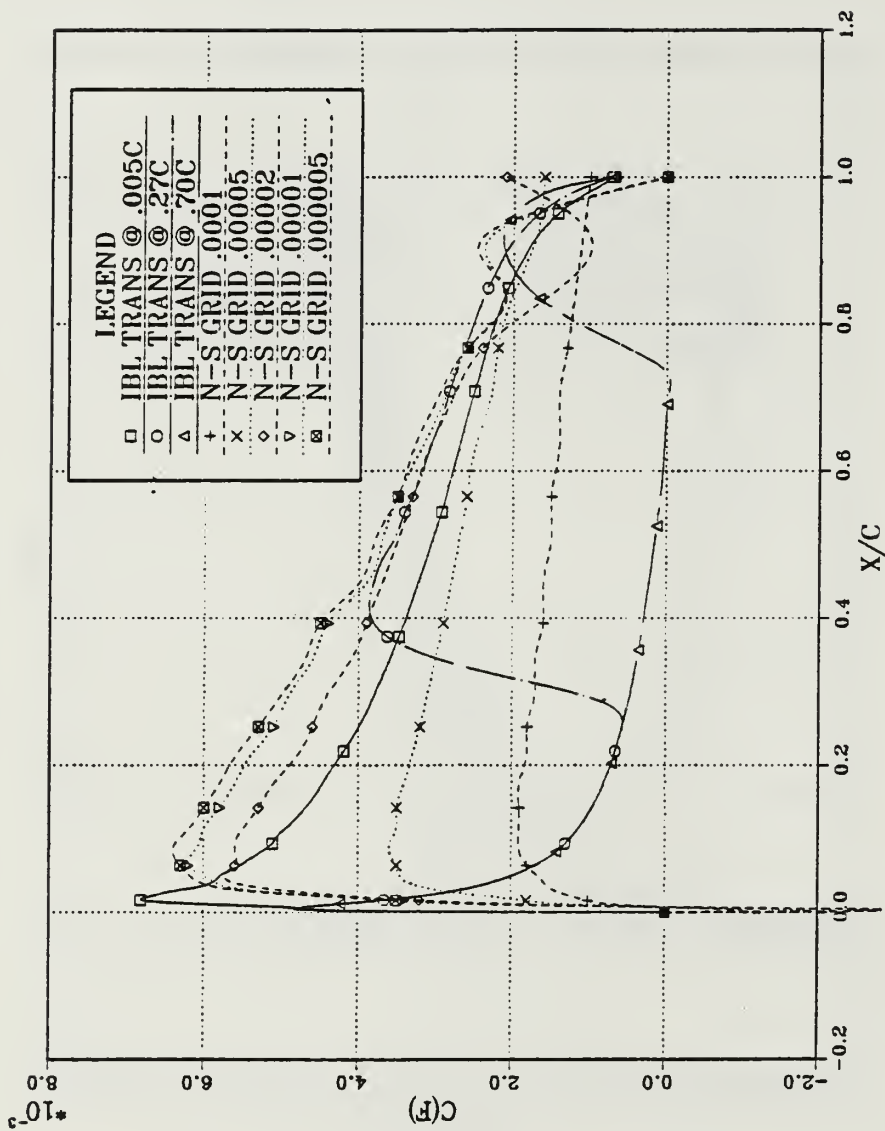


Figure 7.6  $C_f$  vs  $x/c$ ;  $Re = 6M$ ,  $AOA = 0$ ,  $N-S M = .3$

turbulent flow or allows the option to have the code compute transition [Ref. 30]. Figure 7.6 plots  $C_f$  for the NACA 0012 airfoil at a Reynolds number of 6 million at zero degrees angle of attack for eight cases, three using the Cebeci IBL code and five using the results of the Sankar N-S code:

#### Cebeci IBL Code

- 1) turbulent flow; transition at .005c
- 2) computed transition at .27c
- 3) laminar flow; transition at .70c

#### Sankar N-S code

- 4) first grid point at .0001c
- 5) first grid point at .00005c
- 6) first grid point at .00002c
- 7) first grid point at .00001c
- 8) first grid point at .000005c

The C-grid generates 41 points in the direction, clustering them near the wall and stretching them further from the wall. Specifying the first grid point's location from the wall determines where the grid clustering begins.

This study was repeated for a Reynolds number of 3 million at zero degrees angle of attack in Figure 7.8. Six cases are presented, two using the Cebeci IBL code and four using the results of the Sankar N-S code:



#### Cebeci IBL code

- 1) turbulent flow; transition at .005c
- 2) computed transition at .44c

#### Sankar N-S code

- 3) first grid point at .0001c
- 4) first grid point at .00005c
- 5) first grid point at .00001c
- 6) first grid point at .000005c

Figure 7.8 presents a comparison of five cases for a Reynolds number of 15 million at zero degrees angle of attack:

#### Cebeci IBL Code

- 1) turbulent flow, transition at .005c
- 2) specified transition at .70c

#### Sankar N-S code

- 3) first grid point at .0001c
- 4) first grid point at .00005c
- 5) first grid point at .00002c

Velocity profiles are plotted in Figures 7.9 through 7.17. Figures 7.9 through 7.12 show velocity profiles for the conditions of Figure 7.6: Reynolds number = 6 million, angle of attack = 0, N-S Mach = .3. Figure 7.9 is the IBL velocity profile computed when transition is specified at .005c. Figure 7.10 is the laminar velocity profile resulting from specifying the IBL transition at .70c. Figure 7.11 and 7.12 are the velocity profiles computed when specifying the

# SKIN FRICTION

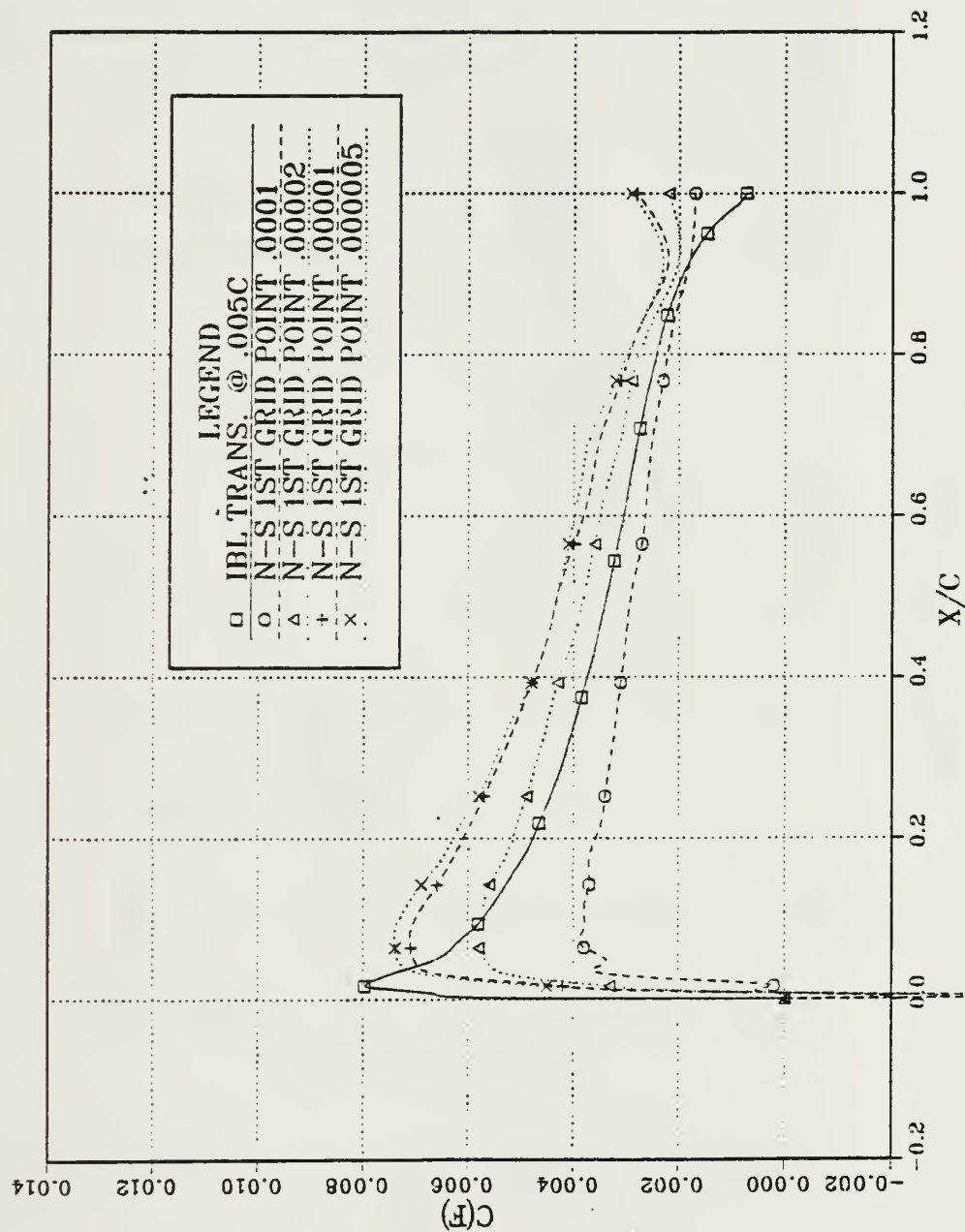


Figure 7.7  $C_f$  vs  $x/c$ ;  $Re = 3M$ ,  $AOA = 0$ ,  $N-S M = .3$

# SKIN FRICTION

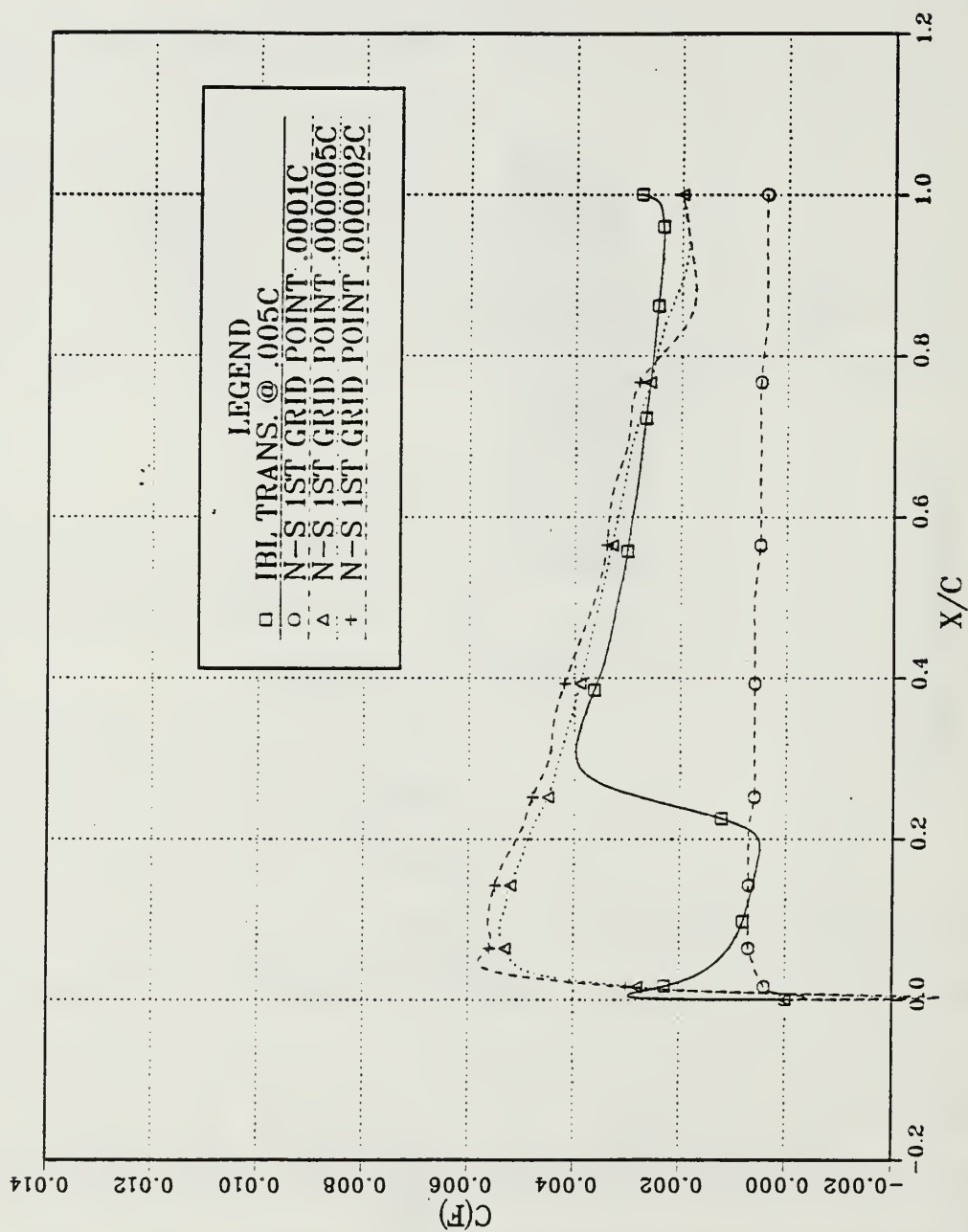


Figure 7.8  $C_f$  vs  $x/c$ ;  $Re = 15M$ ,  $AOA = 0$ ,  $N-S M = .3$

# VELOCITY PROFILES

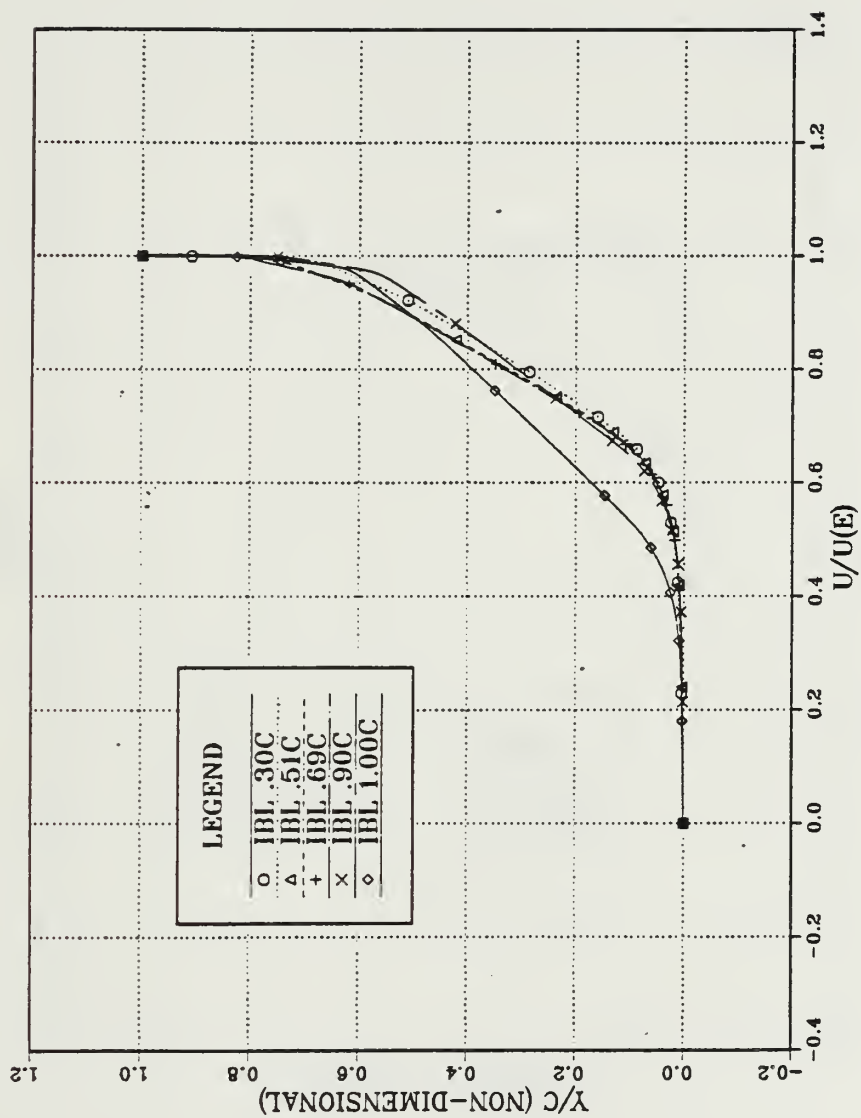


Figure 7.9 Velocity Profile; IBL,  $Re = 6M$ ,  $AOA = 0$ , Trans. .005c

# VELOCITY PROFILES

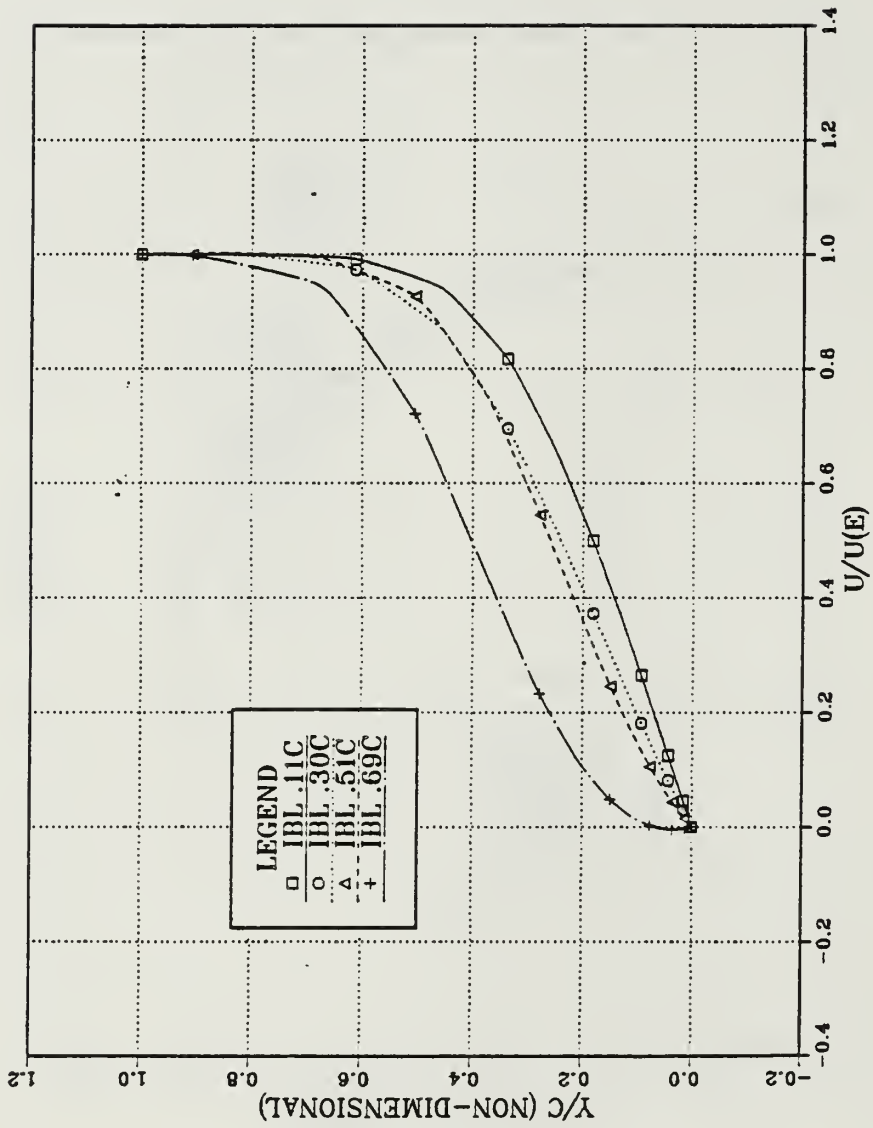


Figure 7.10 Velocity Profile; IBL,  $Re = 6M$ ,  $AOA = 0$ , Trans. 0.70c

# VELOCITY PROFILES

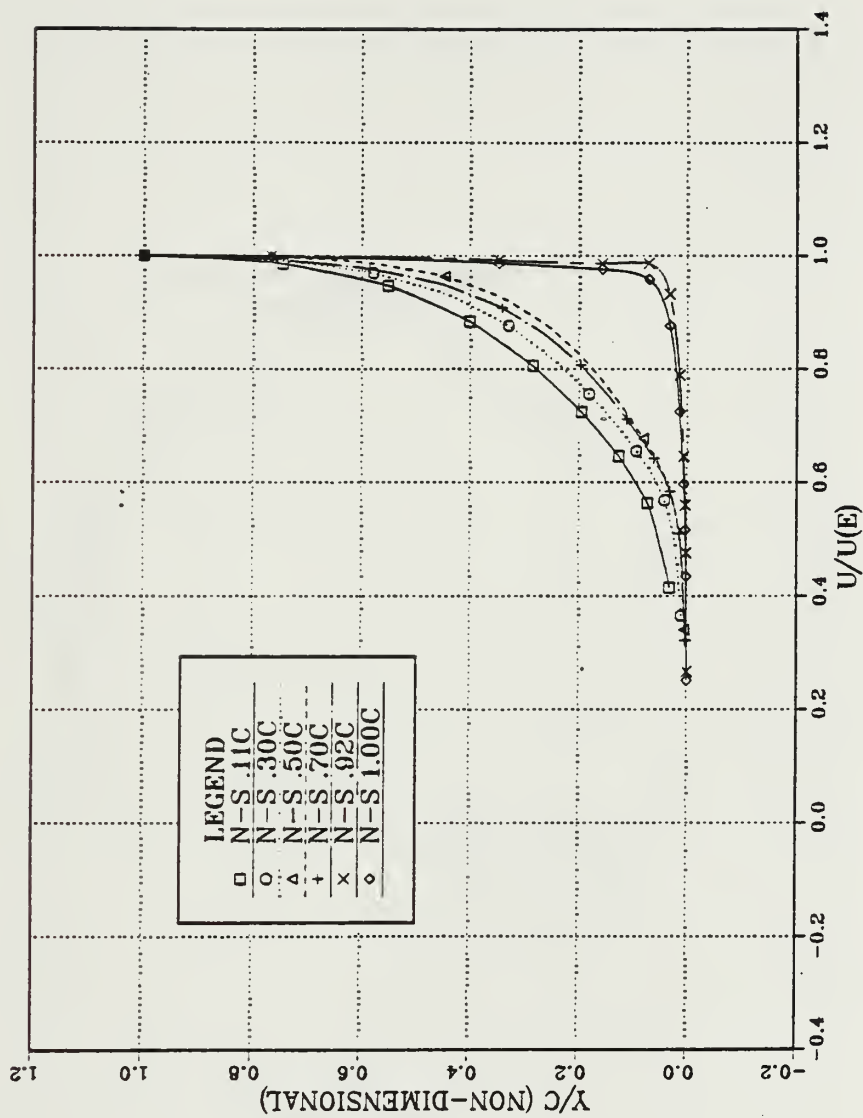


Figure 7.11 Velocity Profile; N-S,  $Re = 6M$ ,  $AOA = 0$ ,  $M = .3$  1st Grid Point .0001c



# VELOCITY PROFILES

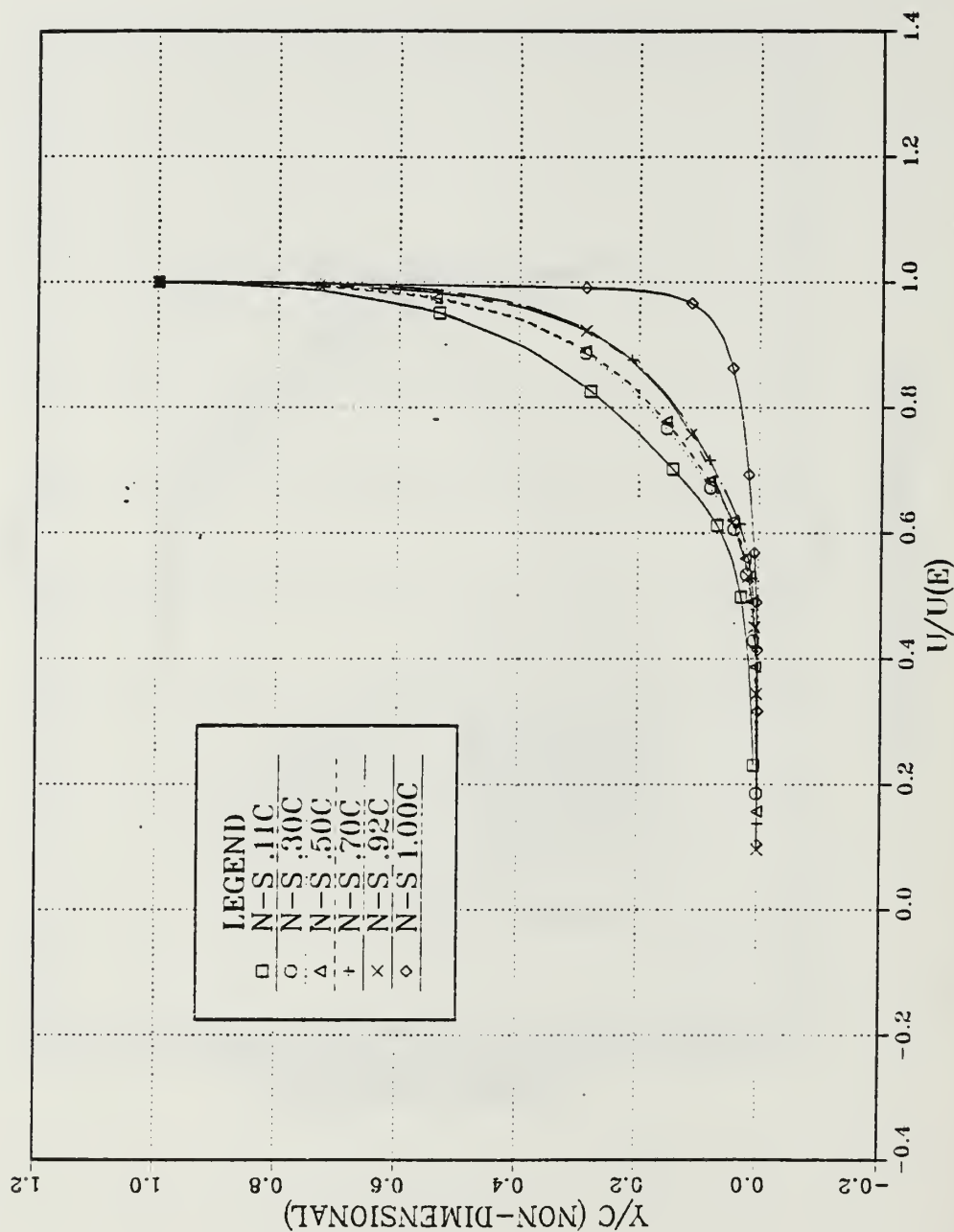


Figure 7.12 Velocity Profile; N-S,  $Re = 6M$ ,  $AOA = 0$ ,  $M = .3$ , 1st Grid Point .00002

# VELOCITY PROFILES

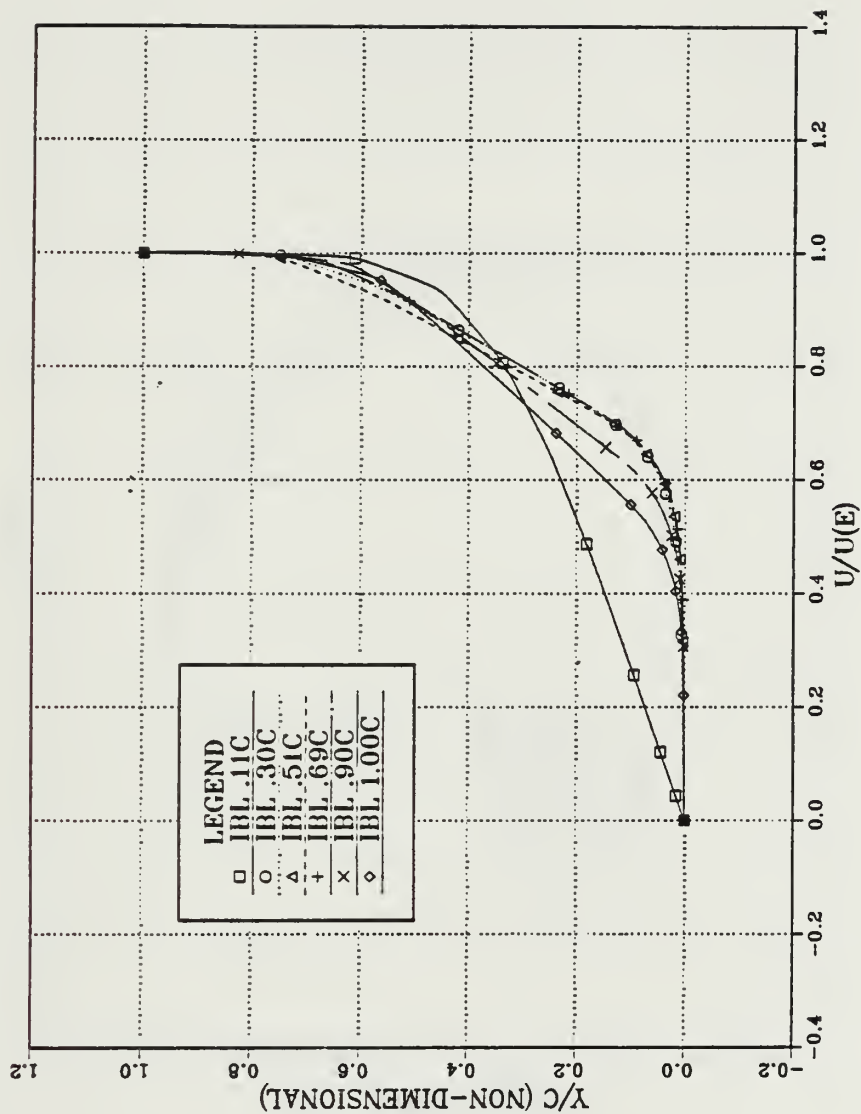


Figure 7.13 Velocity Profile; IBL, Re = 15M, AOA = 0, Trans. .005c

# VELOCITY PROFILES

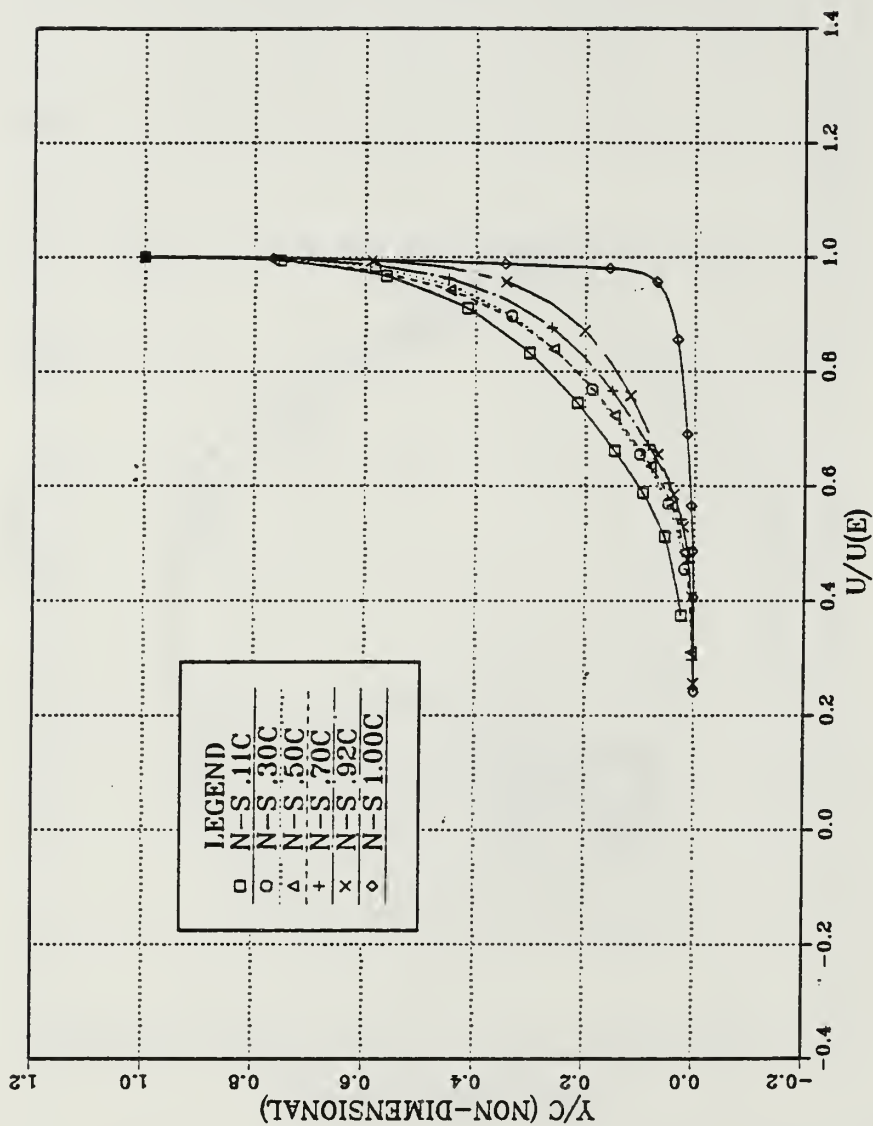


Figure 7.14 Velocity Profile; N-S, Re = 15M, AOA = 0, M = .3, 1st Grid Point .0001c

# VELOCITY PROFILES

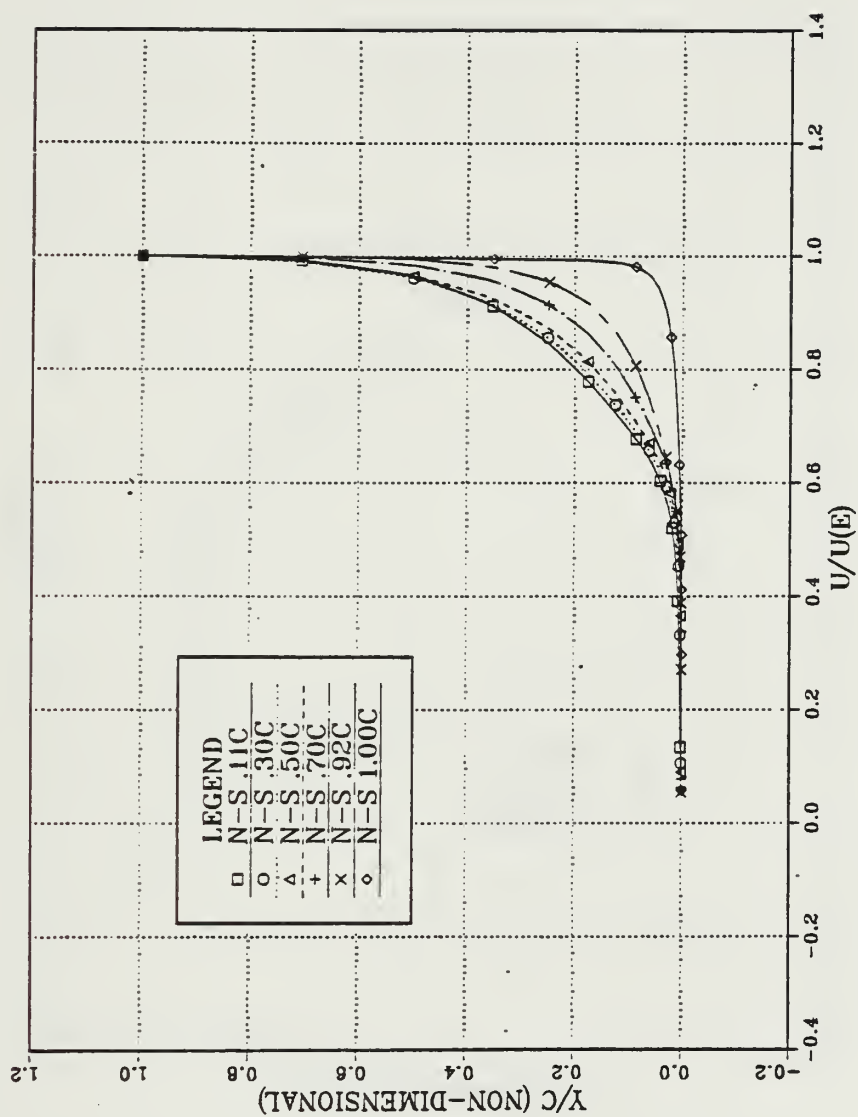


Figure 7.15 Velocity Profile;  $N \cdot S \cdot Re = 15M$ ,  $AOA = 0$ ,  $M = .3$ , 1st Grid Point .000005c

# VELOCITY PROFILES

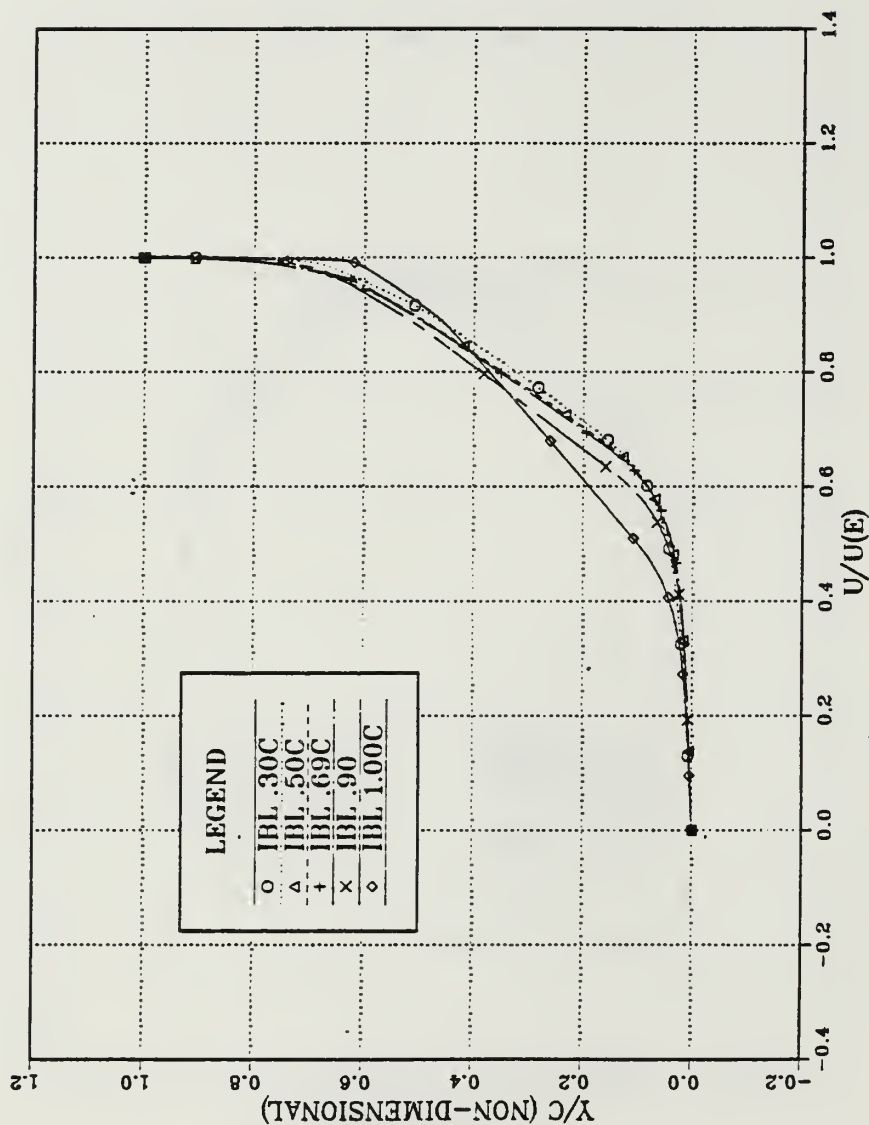


Figure 7.16 Velocity Profile; IBL,  $Re = 1M$ ,  $AOA = 0$ ,  $Trans. = .005c$

# VELOCITY PROFILES

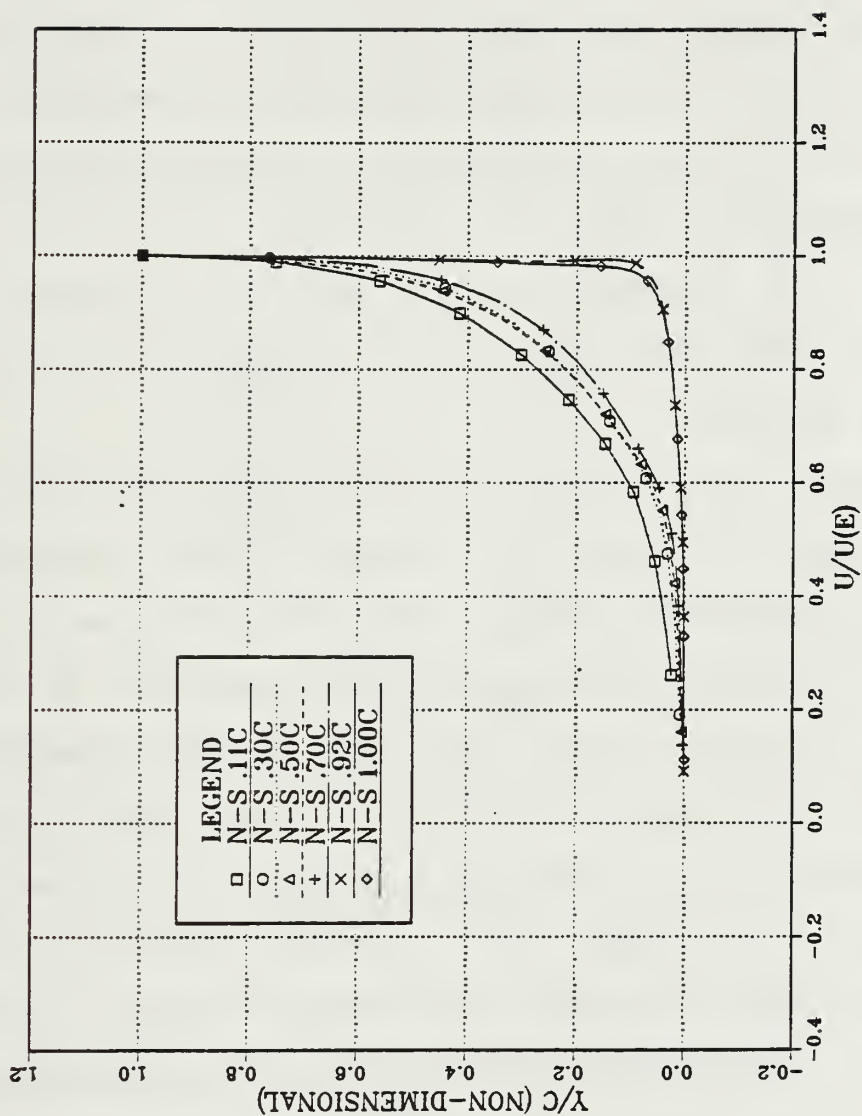


Figure 7.17 Velocity Profile; N-S, Re = 1M, AOA = 0, M = .3, 1st Grid Point .0001c



N-S first grid point from the wall at .0001c and .00002c respectively.

Figures 7.13 through 7.15 are the velocity profiles associated with the conditions of Figure 7.8: Reynolds number = 15 million, angle of attack = 0, and N-S Mach = .30. Figure 7.13 is the IBL turbulent velocity profile, Figure 7.14 is the N-S turbulent velocity profile resulting from specifying the first grid point off of the wall as .0001c, and Figure 7.15 is the N-S velocity profile resulting from specifying the first grid point off of the wall as .000005c.

Figures 7.16 and 7.17 are velocity profiles generated from a Reynolds number of 1 million at zero degrees angle of attack and .30 Mach number. Figure 7.16 is the IBL velocity profile resulting from specifying transition at .005c and Figure 7.17 is the N-S velocity profile resulting from specifying the first grid point at .0001c from the wall.

The results of Figures 7.6 through 7.8 are replotted in Figures 7.18 through 7.20. However, only the turbulent cases and small grid mesh conditions are shown. Figure 7.18 plots the IBL turbulent skin friction at zero degrees angle of attack for Reynolds numbers of 3, 6, and 15 million. Figure 7.19 plots the N-S skin friction at the same conditions as Figure 7.19 for the results of the case with the first grid point specified closest to the wall. Figure 7.20 compares the IBL and N-S results from Figures 7.18 and 7.19.

# SKIN FRICTION

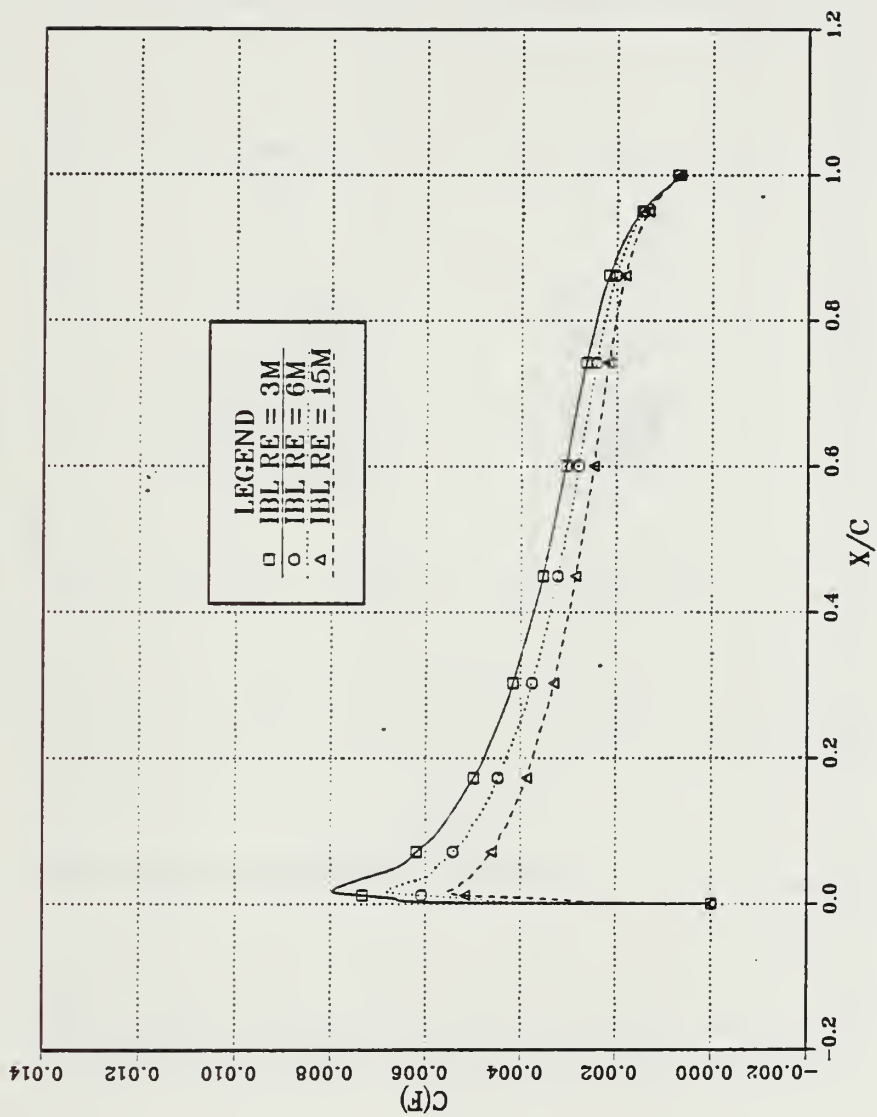


Figure 7.18  $C_f$  vs  $x/c$ ; IBL, AOA = 0, Trans. .005c

# SKIN FRICTION

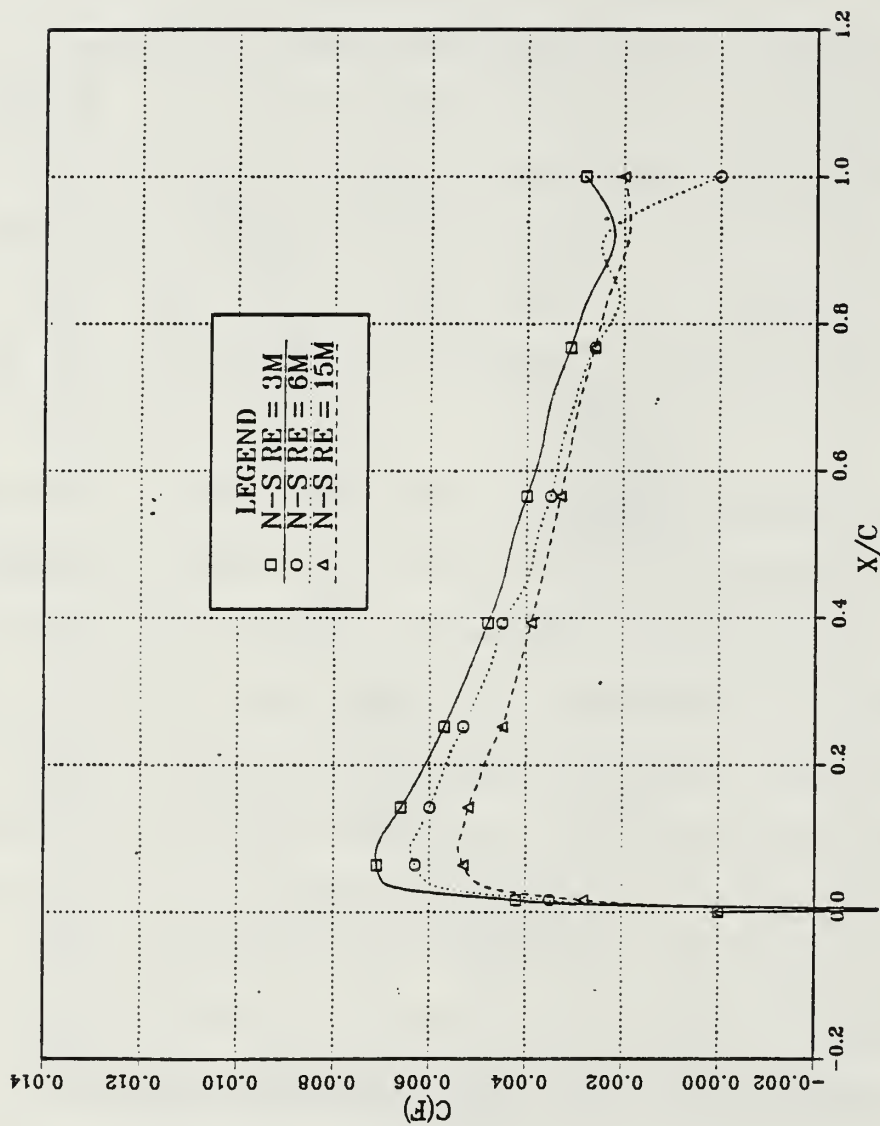


Figure 7.19  $C_f$  vs  $x/c$ ; N-S, AOA = 0,  $M = 0.3$

# SKIN FRICTION

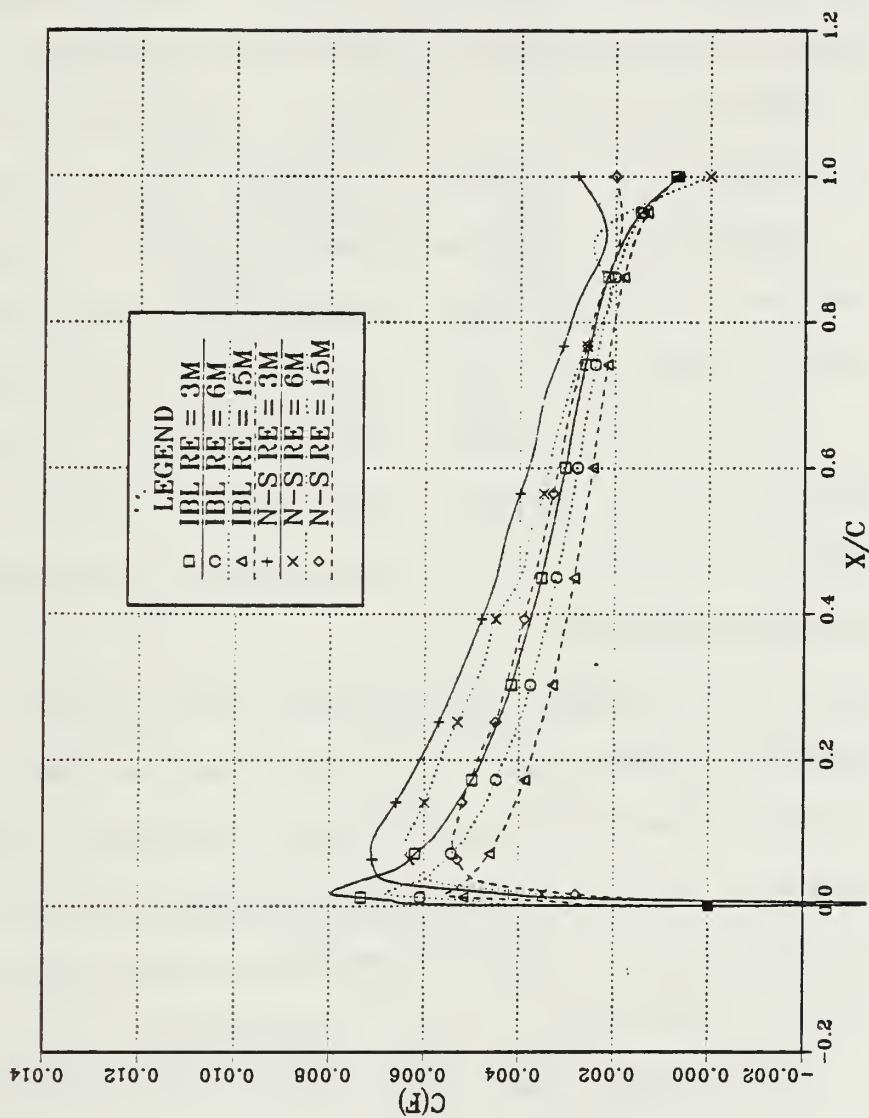


Figure 7.20  $C_f$  vs  $x/c$ ; IBL and N-S,  $Re = 3, 6, 15M$ ,  $AOA = 0$ ,  
N-S  $M = .3$ , IBL Trans. .005c

Next, comparisons between the IBL and N-S skin friction for varying angles of attack were investigated for the conditions of Figure 7.4: Reynolds number = 6 million, Mach = .3, and Figure 7.5: Reynolds number = 1.5 million, Mach = .12. Figures 7.21 through 7.24 are for a Reynolds number of 6 million and a Mach of .3. Figure 7.21 plots the IBL skin friction profile for angles of attack of 0, 4, 8, and 12 degrees. Transition is specified at .005c. Figure 7.22 plots the N-S skin friction for the same angles of attack and a first grid point off the of the wall of .0001c. Figure 7.23 is also the N-S skin friction, but the first grid point off of the wall is specified at .00001c. Figure 7.24 compares the IBL and N-S skin friction profiles for 12 degrees angle of attack.

Figures 7.25 through 7.28 present skin friction profiles for a Reynolds number of 1.5 million and a Mach of .12. Figure 7.25 is the IBL turbulent skin friction (transition is specified at .005c). Figures 7.26 and 7.27 are the N-S skin friction profiles computed when the first grid point is specified at .0001c and .00005c, respectively. Figure 7.28 compares the IBL and N-S skin friction profiles for 6 degrees angle of attack.

# SKIN FRICTION

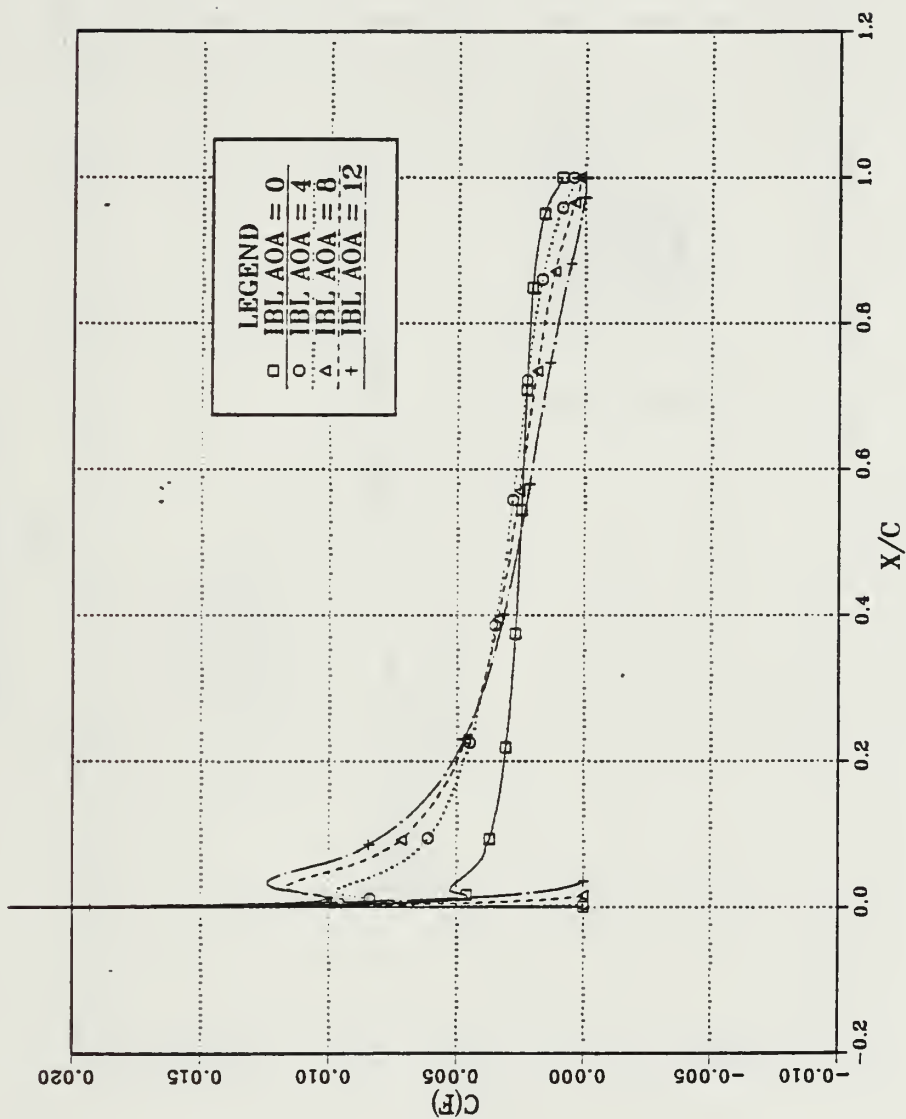


Figure 7.21  $C_f$  vs  $x/c$ ; IBL,  $Re = 6M$ , Trans. .005c



# SKIN FRICTION

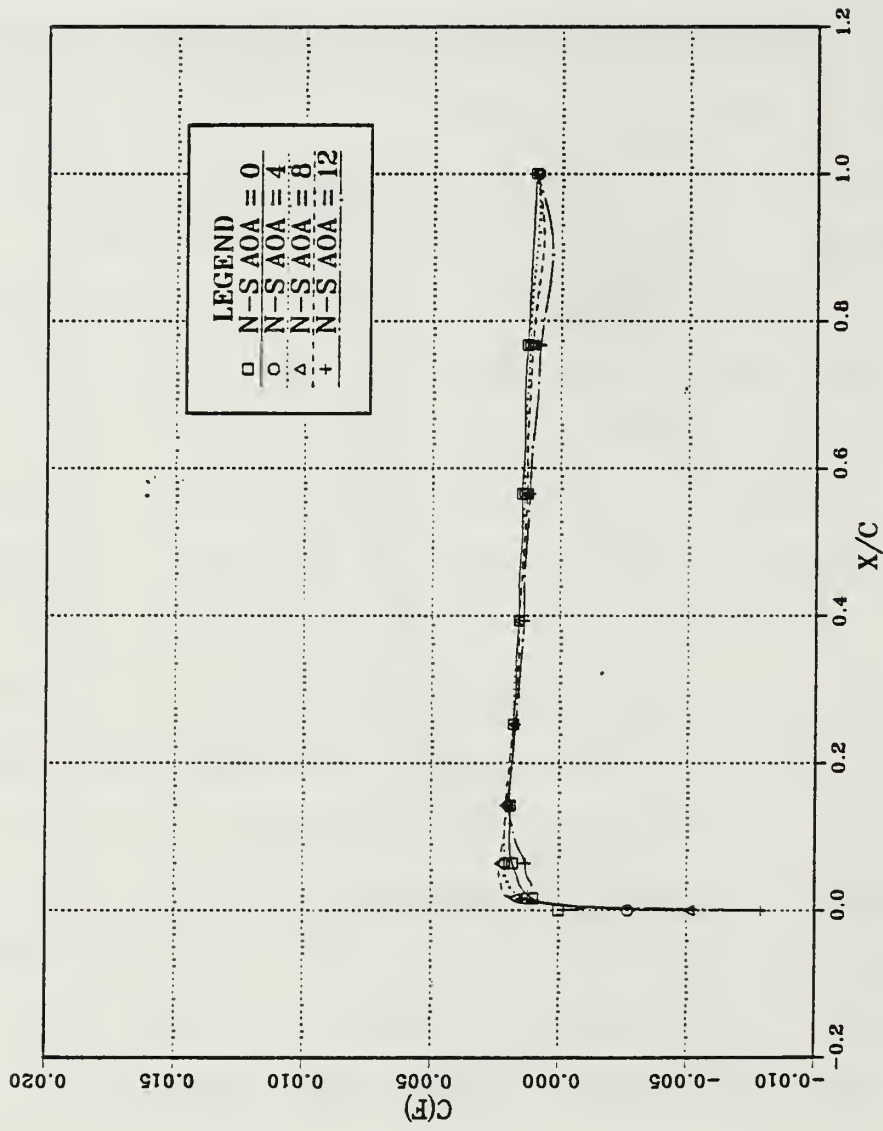


Figure 7.22  $C_f$  vs  $x/c$ ; N-S,  $Re = 6M$ ,  $M = .3$ , 1st Grid Point .0001c

# SKIN FRICTION

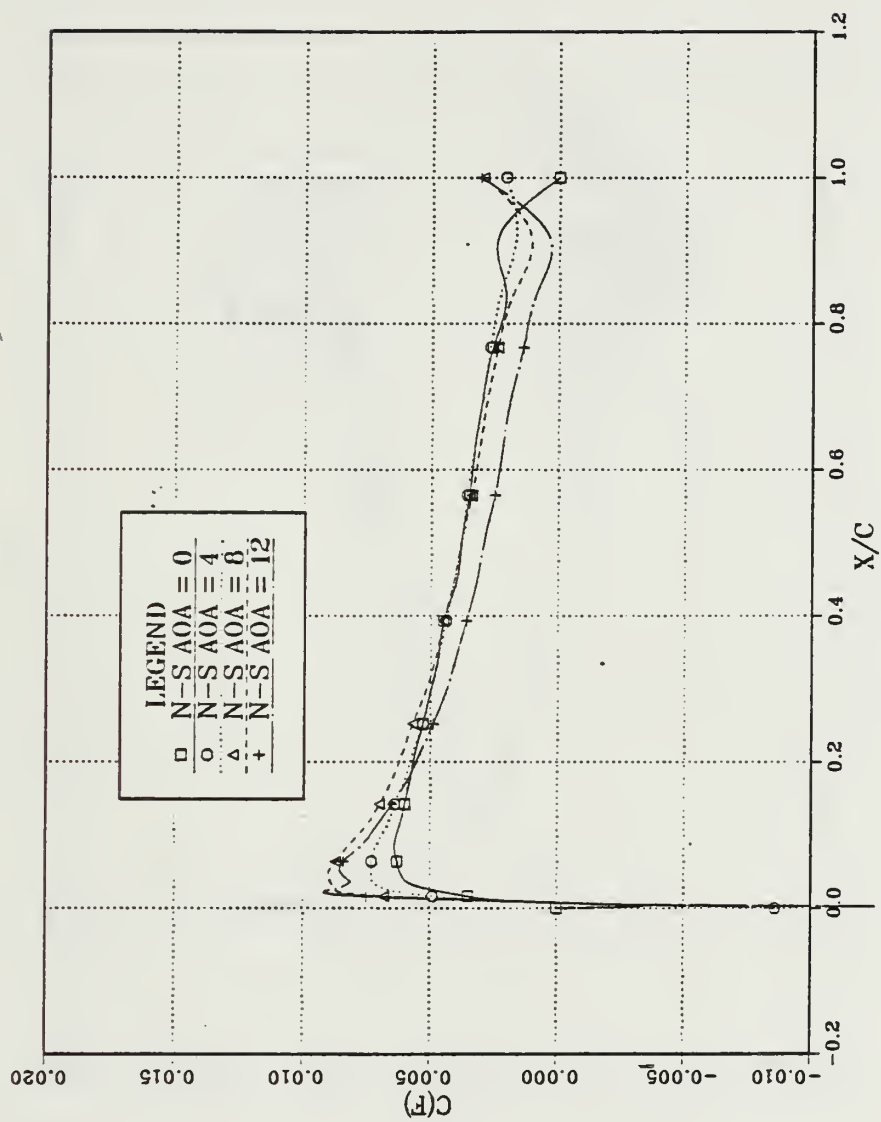


Figure 7.23  $C_f$  vs  $x/c$ ; N-S,  $Re = 6M$ ,  $M = .3$ , 1st Grid Point .00001c

# SKIN FRICTION

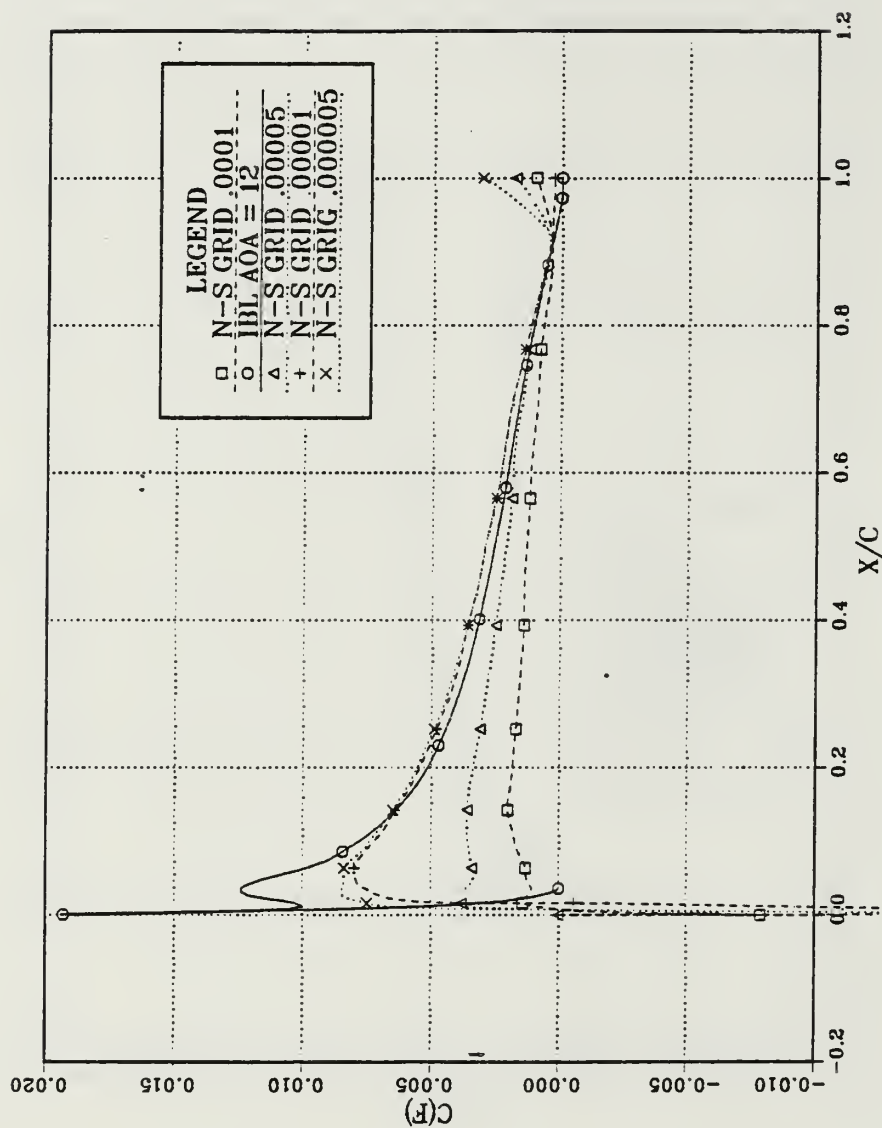


Figure 7.24  $C_f$  vs  $x/c$ ; IBL and N-S,  $Re = 6M$ ,  $AOA = 12$ ,  $N-S M = .3$ , IBL Trans. .005c

# SKIN FRICTION

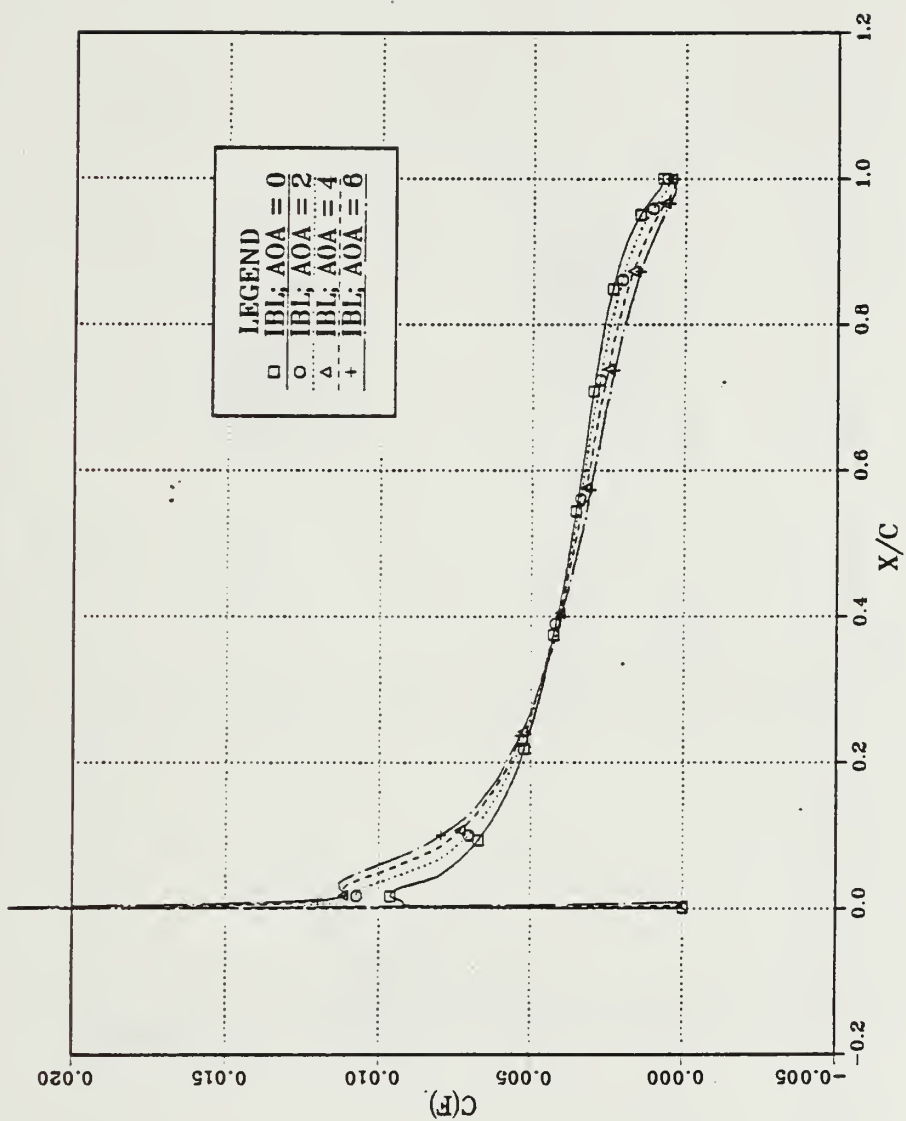


Figure 7.25  $C_f$  vs  $x/c$ ; IBL;  $Re = 1.5M$ ,  $Trans. = 0.005c$

# SKIN FRICTION

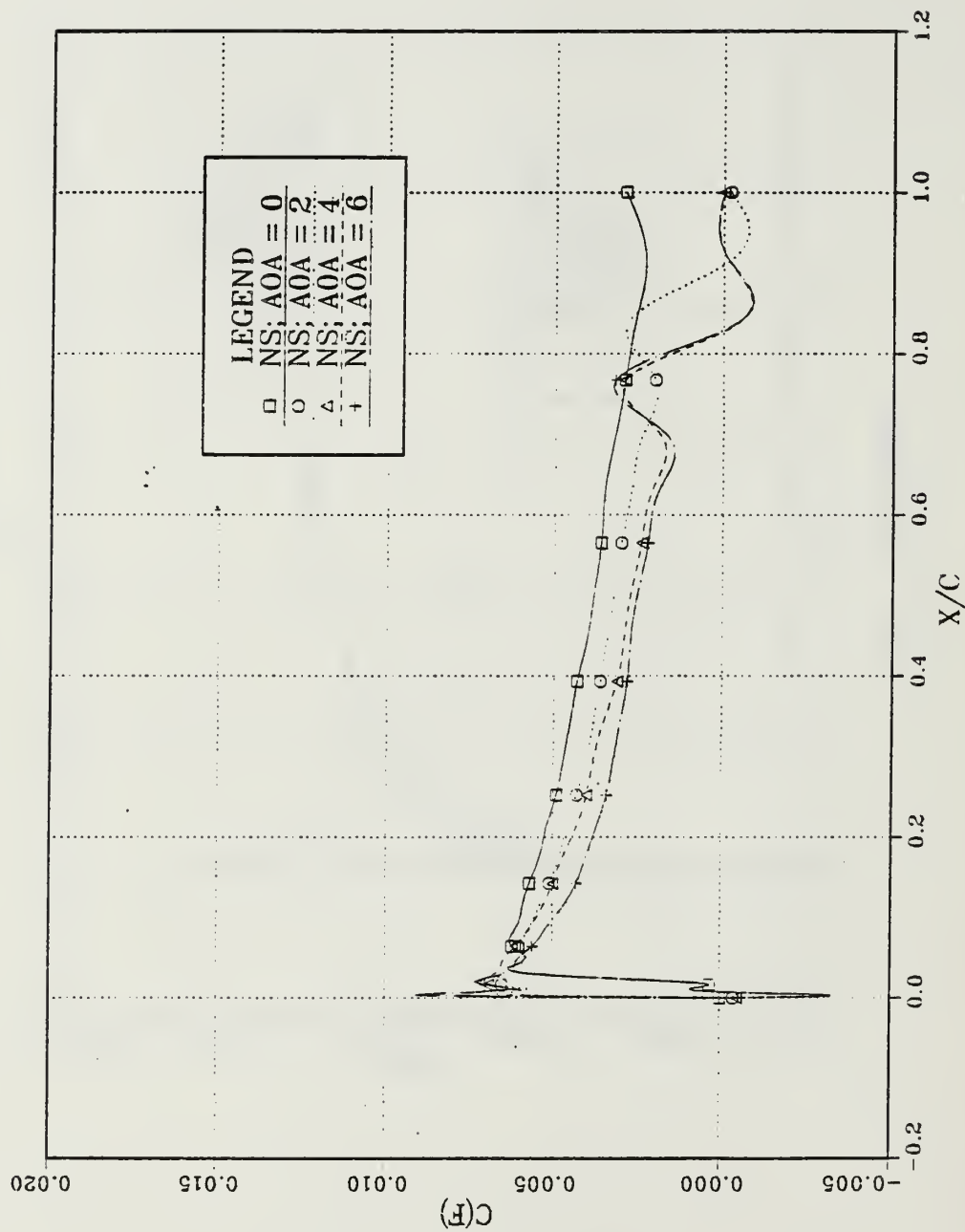


Figure 7.26  $C_f$  vs  $x/c$ ; N-S;  $Re = 1.5M$ ,  $M = .12$ , 1st Grid Point .0001

# SKIN FRICTION

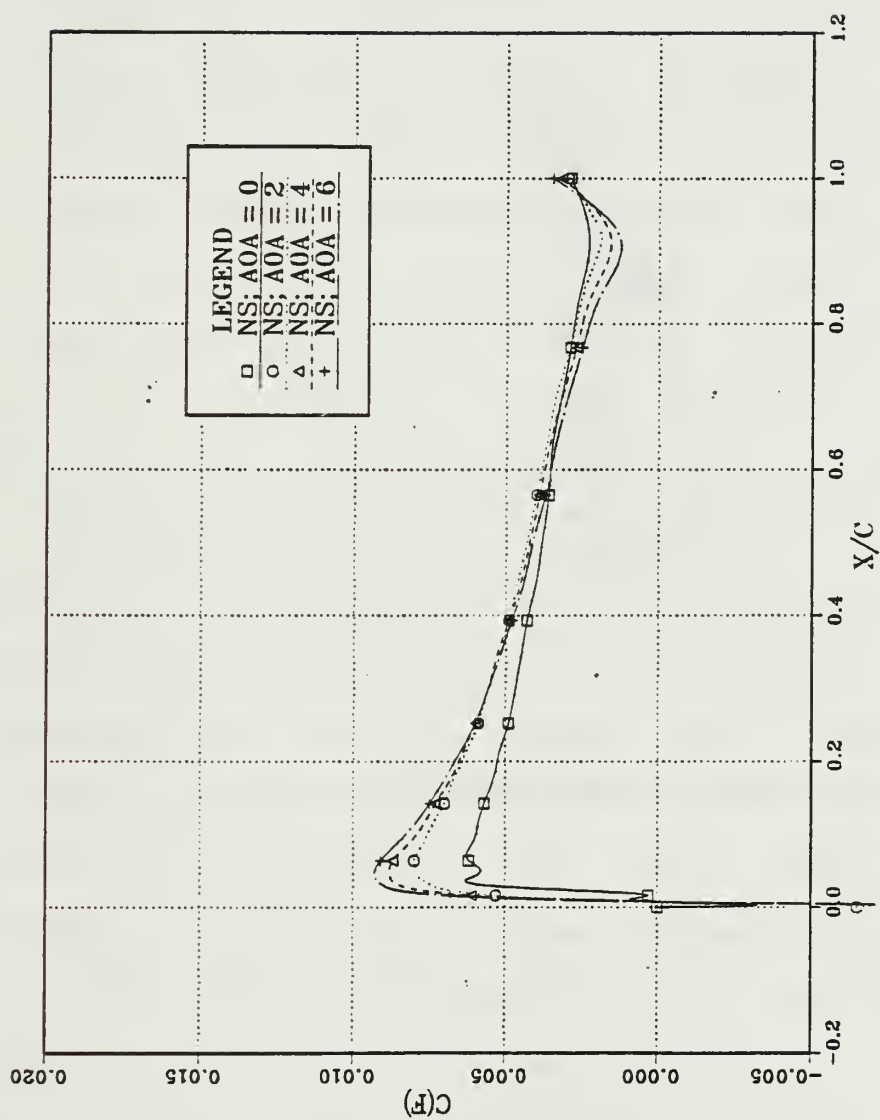


Figure 7.27  $C_f$  vs  $x/c$ ; N-S;  $Re = 1.5M$ ,  $M = .12$ , 1st Grid Point .00005



# SKIN FRICTION

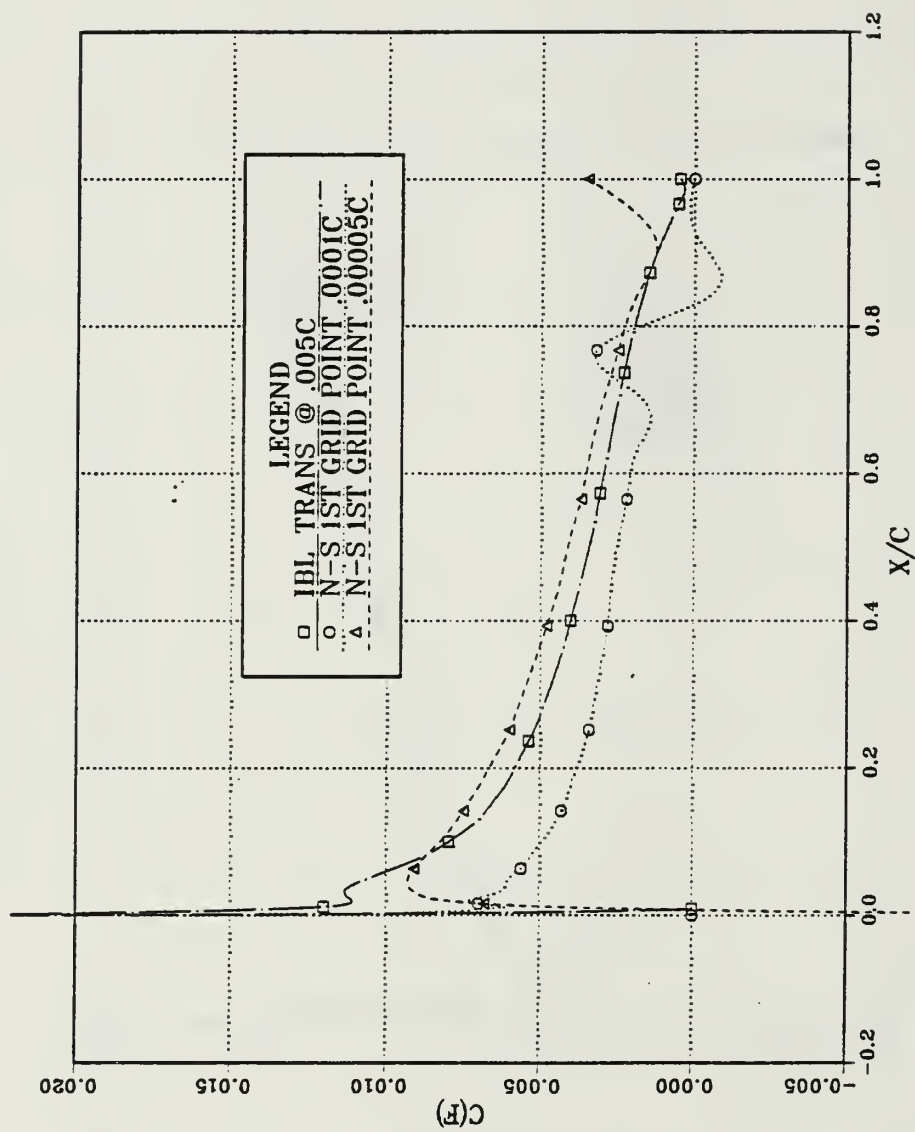


Figure 7.28  $C_f$  vs  $x/c$ ; IBL and N-S,  $Re = 1.5M$ ,  $AOA = 6^\circ$ , N-S  $M = .12$ , IBL Trans.  $.005c$

## VIII. RESULTS AND DISCUSSION

The Sankar N-S code has been compared to the Cebeci IBL code. Integrated values that are not strongly influenced by viscosity, such as coefficients of lift and pressure, correlate well, as shown in Figures 7.1 through 7.5, and with the pressure coefficients presented in Tang [Ref. 23]. However, the viscosity influenced boundary layer values, such as the coefficients of skin friction and velocity profiles, are very sensitive to the type of flow and the grid size. This is evident in Figures 7.6 through 7.8. The IBL laminar skin frictions are much lower than the turbulent values. Also, the influence of the grid mesh on the ability of the N-S code to compute turbulent values is shown. When the first grid point off of the wall is chosen as .0001c, the resulting skin frictions appear laminar for the 6 million and 15 million cases (Figures 7.6 and 7.8). The lower the Reynolds number, the less sensitive the computations are to grid size, as can be seen by comparing the IBL and N-S skin friction values of a Reynolds number of 3 million (Figure 7.7). In all cases, specifying the first grid point closer to the wall positions more points in the boundary layer. For Figure 7.6, when the first grid point from the wall is specified at .0001c, 9 points are located in the boundary layer at 10% chord, 16 points at 50% chord,

and 29 points at the trailing edge. In comparison, when the first grid point from the wall is specified at  $.000005c$ , 13 points are located in the boundary layer at 10% chord, 19 points at 50% chord, and 29 points at the trailing edge of the airfoil.

When the influence on skin friction of subsequent grid refinements in the N-S code is negligible, the N-S skin frictions are substantially greater than the values computed by the IBL code when transition is specified at  $.005c$ . See Figure 7.20. It is of interest to note, however, the higher coefficients of skin friction evident when transition is delayed in the IBL code as in Figure 7.6.

The velocity profiles, Figures 7.9 through 7.17, vary little in the turbulent cases, regardless of grid size or Reynolds number. The shape of the profiles varies between the IBL and N-S cases, but both exhibit turbulent velocity profiles. There is a discrepancy between the skin friction and velocity profile results computed by the N-S code when the first point off of the wall is  $.0001c$ . The coefficients of skin friction indicate laminar flow, whereas the velocity profiles are turbulent. A laminar velocity profile, Figure 7.10, is calculated using the IBL code (Reynolds number of 6 million, 0 degrees angle of attack).

The influence of the grid mesh is again evident in the angle of attack studies, Figures 7.21 through 7.28. The coefficients of skin friction for the higher Reynolds number

of 6 million seem to not be dependent on angle of attack if the grid points are not located sufficiently close to the wall. This is not evident for the lower Reynolds number of 1 million. The N-S skin friction values, when no longer influenced by grid size, are again higher than the fully turbulent values computed by the Cebeci IBL code, as seen in Figures 7.24 and 7.28.

Varying the artificial viscosity in the Sankar N-S code did not vary the solution of the skin friction. However, all cases were run with the first grid point .0001c from the wall, so no conclusion should be drawn. If the number of time steps was exceedingly large (8000 steps) for zero degrees angle of attack, the pressure and skin friction profiles began to indicate separated flow.

Angle of attack studies using the Sankar N-S code required a large number of time steps (approximately 7000) before the coefficient of lift converged to realistic values, regardless of the first grid point off of the wall specified. The coefficient of friction values stabilized relatively quickly, within 2000 to 3000 time steps. Several computer runs at each angle of attack and Reynolds number were then required to determine when specification of the first grid point off of the wall no longer influenced the skin friction values computed. At this point, the results were assumed to be converged.

The IBL code took less than 16 iterations to converge, regardless of the Reynolds number chosen or the angle of attack. Very low Reynolds numbers would require more iterations, however.

## IX. CONCLUSIONS AND RECOMMENDATIONS

Both the Sankar Navier-Stokes Code and the Cebeci Interactive Boundary Layer code show reasonable results for high Reynolds number, incompressible steady flows over a NACA 0012 airfoil. The discrepancy in skin frictions should be resolved and the influence of dissipation on the skin friction investigated. These steady-state results should then be extended to other airfoils and low Reynolds flows to determine the effect of increased viscosity on the codes. The effect of transition on the velocity profiles and the skin friction is modeled in the Cebeci IBL code; however, the lack of a transition model and a smearing function in the Sankar N-S code limits its ability to model most experimental flows, especially at low Reynolds numbers. Also of importance is the wake influence, which has not been addressed in this report, and the growth of the boundary layer along the airfoil. Since the velocity profile results are presented non-dimensionally, this trend is not evident. The difference in profile shapes generated from the N-S code and the IBL code could be resolved better if the actual boundary layer profile, rather than a non-dimensionalized profile, is used.

Neither code was extensively compared to experimental results for skin frictions or velocity profiles. This is,



of course, a criterion in determining the accuracy of the codes. The cost and time considerations associated with running the codes indicate that, at the present, for steady-state runs, the IBL code is more effective. The N-S runs were submitted to the NASA X-MP Cray, where waiting times of 24 hours before the program was executed was common. Execution times ran between 10 and 40 minutes, at a cost of \$1000 per hour. In comparison, the IBL program normally was completed in 10 to 30 minutes on the Naval Postgraduate School IBM mainframe, for less than \$50.

The N-S code is a very effective tool for calculating dynamic stall characteristics. Its capability as a general flow solver, however, is limited in comparison to the IBL technique in terms of cost and time constraints.

## LIST OF REFERENCES

1. McCroskey, W.J. and McAlister, K.W., et al., "Dynamic Stall on Advanced Airfoil Sections," J. American Helicopter Society, V. 26, No. 3, pp. 40-50, July 1981.
2. Cebeci, T., "Airfoils with Separation and the Resulting Wakes," J. Fluid Mechanics, V. 163, pp. 323-347, 1986.
3. American Institute of Aeronautics and Astronautics Paper 85-0129, "Numerical Solution of Unsteady Viscous Flow Past Rotor Sections," by N.L. Sankar and W. Tang, January 1985.
4. Beam, R.M., and Warming, R.F., "An Implicit Factored Scheme for the Compressible Navier-Stokes Equations," AIAA Journal, V. 16, No. 4, pp. 393-402, April 1978.
5. Steger, J.L., "Implicit Finite-Difference Simulation of Flow about Arbitrary Two-Dimensional Geometries," AIAA Journal, V. 16, No. 7, pp. 679-686, July 1978.
6. American Institute of Aeronautics and Astronautics Paper 87-0495, "Boundary Layer Measurements on an Airfoil at Low Reynolds Numbers," by M. Brandal and T.J. Mueller, January 1987.
7. Marchman, J.F., "Aerodynamic Testing at Low Reynolds Numbers," J. Aircraft, V. 24, No. 2, pp. 107-114, February 1987.
8. National Aeronautics and Space Administration Technical Memorandum 84245, "An Experimental Study of Dynamic Stall on Advanced Airfoil Sections," by W.J. McCroskey, K.W. McAlister, L.W. Carr, and S.L. Pucce, July 1982.
9. American Institute of Aeronautics and Astronautics Paper 87-0242, "A Study of the Laminar Separation Bubble on an Airfoil at Low Reynolds Numbers Using Flow Visualization Techniques," by G.S. Schmidt and T.J. Mueller, January 1987.
10. McCroskey, W.J., Carr, L.W., and McAlister, K.W., "Dynamic Stall Experiments on Oscillating Airfoils," AIAA Journal, V. 14, No. 1, pp. 57-63, January 1976.

11. Cebeci, T., Editor, Numerical and Physical Aspects of Aerodynamic Flows, Vols. I-III, Springer-Verlag, New York, 1982, 1984, 1985.
12. Subroto, P.H., Viscous/Inviscid Interaction Analyses of the Aerodynamic Performance of the NACA 65-213 Airfoil, Master's Thesis, Naval Postgraduate School, Monterey, California, March 1987.
13. Valdes, James, Dynamic Stall Calculations Using a Navier-Stokes Solver, Master's Thesis, Naval Postgraduate School, Monterey, California, December 1986.
14. Daily, J.W. and Harleman, D.R., Fluid Dynamics, Addison-Wesley Publishing Company, Inc., 1966.
15. Shapiro, A.H., The Dynamics and Thermodynamics of Compressible Fluid Flow, Vol. 1, John Wiley and Sons, Inc., 1953.
16. Schlichting, H., Boundary Layer Theory, 7th ed., McGraw-Hill, Book Co., 1979.
17. Moran, J., An Introduction to Theoretical and Computational Aerodynamics, John Wiley and Sons, Inc., 1984.
18. Patel, V.C., Rodi, W., and Scheuerer, G., "Turbulence Models for Near-Wall and Low Reynolds Number Flows: A Review," AIAA Journal, V. 23, No. 9, pp. 1308-1319.
19. Cebeci, T., Chang, K.C., Li, C., and Whitelaw, J.H., "Turbulence Models for Wall Boundary Layers," AIAA Journal, V. 23, No. 3, pp. 359-361, March 1986.
20. Cebeci, T. and Smith, A., Analysis of Turbulent Boundary Layers, Academic Press, 1974.
21. York, B. and Knight, D., "Calculation of Two-Dimensional Turbulent Boundary Layers Using the Baldwin-Lomax Model," AIAA Journal, V. 23, No. 12, pp. 1849-1851, December 1985.
22. American Institute of Aeronautics and Astronautics Paper 81-1289, "Dynamic Stall of NACA 0011 Airfoil in Turbulent Flow--Numerical Study," by Y. Tasner and N.L. Sankar, June 1981.
23. Tang, W., Numerical Solutions of Unsteady Flow Past Rotor Sections, Ph.D. Thesis, Georgia Institute of Technology, Atlanta, Georgia, August 1986.

24. Jameson, A., "Iterative Solution of Transonic Flows over Airfoils and Wings, Including Flows at Mach 1," Communications on Pure and Applied Mathematics, V. xxvii, pp. 283-309, 1974.
25. Howard, R., Class notes from High Speed Aerodynamics, Naval Postgraduate School, Monterey, California, Winter 1987.
26. Murman, E. and Cole, J., "Calculation of Plane Steady Transonic Flow," AIAA Journal, V. 9, No. 1, pp. 114-121, January 1971.
27. Cebeci, T., Wang, G.S., Chang, K.C., and Choi, J., "Recent Developments in the Calculation of Flow over Low Reynolds Number Airfoils," paper presented at the International Conference on Aerodynamics at Low Reynolds Numbers, held at the Royal Aeronautical Society, London, England, 16-17 October 1986.
28. Keller, H.B., "Accurate Difference Methods for Two-Point Boundary Value Problems," SIAM J. Numerical Analysis, V. 11, No. 2, pp. 305-320, April 1974.
29. Paik, S.W., Application of the Viscous Inviscid Interaction Methods to the Analysis of Airfoil Flows at Low Reynolds Numbers, Master's Thesis, Naval Postgraduate School, Monterey, California, December 1986.
30. Anderson, D.A., Tannehill, J.C. and Pletcher, R.H., Computational Fluid Mechanics and Heat Transfer, McGraw-Hill (Hemisphere Publishing Co.), 1984.
31. Halsey, N.D., "Potential Flow Analysis of Multielement Airfoils Using Conformal Mapping," AIAA Journal, V. 17, No. 12, pp. 1281-1288, December 1979.



INITIAL DISTRIBUTION LIST

	No. Copies
1. Defense Technical Information Center Cameron Station Alexandria, Virginia 22304-6145	2
2. Library, Code 0142 Naval Postgraduate School Monterey, California 93943-5002	2
3. Chairman, Code 67 Department of Aeronautical Engineering Naval Postgraduate School Monterey, California 93943-5004	5
4. Lawrence W. Carr Fluid Mechanics Laboratory Mail Stop 260-1 NASA Ames Research Center Moffett Field, California 94035	1
5. N.L. Sankar School of Aerospace Engineering Georgia Institute of Technology Atlanta, Georgia 30332	1
6. Tuncer Cebeci Director, Center for Aerodynamic Research California State University Long Beach, California 90840	1
7. Campbell Henderson Head, Aircraft Performance Analysis Branch Code 6051 Naval Air Development Center Warminster, Pennsylvania 18974-5000	2
8. Lisa J. Cowles Code 6051 Naval Air Development Center Warminster, Pennsylvania 18974-5000	10











Thesis  
C756965 Cowles  
c.1 High Reynolds number,  
low Mach number, steady  
flow field calculations  
over a NACA 0012 airfoil  
using Navier-Stokes and  
Interactive Boundary  
Layer theory.



thesC756965

High Reynolds number, low Mach number, s



3 2768 000 77208 1

DUDLEY KNOX LIBRARY